Title: Simulation of the clinical and pathological manifestations of Coronavirus Disease 2019 (COVID-19) in golden Syrian hamster model: implications for disease pathogenesis and transmissibility

Authors: Jasper Fuk-Woo Chan[1,2,3,a], Anna Jinxia Zhang[1,a], Shuofeng Yuan[1,a], Vincent Kwok-Man Poon[1], Chris Chung-Sing Chan[1], Andrew Chak-Yiu Lee[1], Wan-Mui Chan[1], Zhimeng Fan[1], Hoi-Wah Tsoi[1], Lei Wen[1], Ronghui Liang[1], Jianli Cao[1], Yanxia Chen[1], Kaiming Tang[1], Cuiting Luo[1], Jian-Piao Cai[1], Kin-Hang Kok[1], Hin Chu[1], Kwok-Hung Chan[1], Siddharth Sridhar[1,2,3], Zhiwei Chen[1], Honglin Chen[1], Kelvin Kai-Wang To[1,2,3], Kwok-Yung Yuen[1,2,3]

[a]J.F-W.C., A.J.Z., and S.Y. contributed equally to this work.

Affiliations:

[1]State Key Laboratory of Emerging Infectious Diseases, Carol Yu Centre for Infection, Department of Microbiology, Li Ka Shing Faculty of Medicine, The University of Hong Kong, Pokfulam, Hong Kong Special Administrative Region, China.

[2]Department of Clinical Microbiology and Infection Control, The University of Hong Kong-Shenzhen Hospital, Shenzhen, China.

[3]Department of Microbiology, Queen Mary Hospital, Pokfulam, Hong Kong Special Administrative Region, China.

Correspondence: Kwok-Yung Yuen (kyyuen@hku.hk), State Key Laboratory of Emerging Infectious Diseases, Carol Yu Centre for Infection, Department of Microbiology, Li Ka Shing

Faculty of Medicine, The University of Hong Kong, Pokfulam, Hong Kong Special Administrative Region, China. Tel: 852-22552402. Fax: 852-28551241.

Summary:

A novel, readily available, and physiological small animal model of Syrian hamster for SARS-CoV-2 infection that recapitulates the clinical, virological, histopathological, and immunological characteristics of human disease was established to study the pathogenesis, transmission, and passive immunisation effect of COVID-19.

ABSTRACT

Background. A physiological small animal model that resembles COVID-19 with low mortality is lacking.

Methods. Molecular docking on the binding between angiotensin-converting enzyme 2 (ACE2) of common laboratory mammals and the receptor-binding domain of the surface spike protein of SARS-CoV-2 suggested that the golden Syrian hamster is an option. Virus challenge, contact transmission, and passive immunoprophylaxis were performed. Serial organ tissues and blood were harvested for histopathology, viral load and titre, chemokine/cytokine assay, and neutralising antibody titre.

Results. The Syrian hamster could be consistently infected by SARS-CoV-2. Maximal clinical signs of rapid breathing, weight loss, histopathological changes from the initial exudative phase of diffuse alveolar damage with extensive apoptosis to the later proliferative phase of tissue repair, airway and intestinal involvement with virus nucleocapsid protein expression, high lung viral load, and spleen and lymphoid atrophy associated with marked cytokine activation were observed within the first week of virus challenge. The lung virus titre was between 10^5-10^7 $TCID_{50}$/g. Challenged index hamsters consistently infected naïve contact hamsters housed within the same cage, resulting in similar pathology but not weight loss. All infected hamsters recovered and developed mean serum neutralising antibody titre ≥1:427 fourteen days post-challenge. Immunoprophylaxis with early convalescent serum achieved significant decrease in lung viral load but not in lung pathology. No consistent non-synonymous adaptive mutation of the spike was found in viruses isolated from infected hamsters.

Conclusions. Besides satisfying the Koch's postulates, this readily available hamster model is an important tool for studying transmission, pathogenesis, treatment, and vaccination against SARS-CoV-2.

Keywords: coronavirus; COVID-19; SARS-CoV-2; animal; transmission.

Severe acute respiratory syndrome coronavirus 2 (SARS-CoV-2) is causing a looming pandemic of Coronavirus Disease 2019 (COVID-19).[1] This newly emerged coronavirus belongs to the genus *Betacoronavirus* which also includes the highly pathogenic SARS-CoV and Middle East respiratory syndrome coronavirus (MERS-CoV).[2] Phylogenetic analysis suggested that all three coronaviruses have likely originated from bats.[3] SARS-CoV-2 was first identified in patients with atypical pneumonia geographically linked to a wet market with wild animal trade in Wuhan, China. The virus is highly transmissible among humans with clusters occurring among close contacts in family, church, community, cruise ship, nursing home, and hospital settings.[2,4-7] Within just three months, >100,000 cases of COVID-19 with >3000 deaths have been reported globally in >100 countries/territories.[8] As readily available and suitable experimental animal models are lacking, the major route of transmission is speculated to be through respiratory droplets, direct or indirect contact with other infectious bodily fluids, such as saliva, faeces, tears, and blood.

Recent data showed that the clinical severity of COVID-19 ranges widely from asymptomatic infection to fatal disease. In children, COVID-19 is usually asymptomatic or mildly symptomatic.[2,9] The majority of immunocompetent adult COVID-19 patients present with fever, respiratory symptoms, and radiological ground-glass lung opacities.[10] In severe cases especially among elderly and immunocompromised patients, besides respiratory failure, extrapulmonary manifestations such as diarrhoea, confusion, hepatic and renal dysfunction, lymphopenia, thrombocytopenia, and elevated inflammatory biomarkers have also been reported.[10] Small animal models that recapitulate the clinical and pathological features of COVID-19 in human are essential tools for studying the pathogenesis, transmission, antiviral treatments, and vaccines for this emerging global health threat. Based on the recent identification

of human angiotensin-converting enzyme 2 (ACE2) as the cell entry receptor of SARS-CoV-2, a transgenic human ACE2 mouse model was preliminarily reported.[11] However, the expression of human ACE2 in these transgenic mice is not physiological and these mice are not readily available. A rhesus macaque model was also reported, but expertise and Biosafety Level-3 facilities to handle non-human primates are scarce.[11] In this study, we established a readily available small animal model for COVID-19 using golden Syrian hamster (*Mesocricetus auratus*). Our *in silico* structural analysis predicted that the hamster ACE2 can bind with SARS-CoV-2 spike glycoprotein receptor-binding domain (RBD) at high binding affinity. The clinical features, viral kinetics, histopathological changes, and immune responses in SARS-CoV-2-infected Syrian hamsters closely mimic those described in many COVID-19 patients. Using this newly established model, we demonstrated the high transmissibility of SARS-CoV-2 among close contact animals.

METHODS

Amino acid and binding energy comparison between human and other mammalian ACE2

Multiple sequence alignment was generated using the human, rhesus macaque, common marmoset, hamster, rabbit, ferret, rat, mouse, pig, and bat ACE2 protein sequences (Uniprot accession numbers Q9BYF1, B6DUF3, F7CNJ6, G1TEF4, A0A1U7QTA1, Q2WG88, Q5EGZ1, Q8R0I0, K7GLM4, and E2DHI7, respectively) with MUSCLE.[12] Missing loop residues in the SARS-CoV-2 spike protein RBD (PDB ID:6VSB) was modelled with I-TASSER.[13] The human ACE2 and SARS-CoV-spike complex structure model (PDB ID:2AJF) was used to model ACE2 and SARS-CoV-2-spike complex by superposition of SARS-CoV-2-RBD to SARS-CoV-RBD. ACE2-spike complexes of SARS-CoV-2 and SARS-CoV were then minimized with Rosetta

Relax application.[14] ACE2-spike interface binding energy was calculated by InterfaceAnalyzer within Rosetta. Interface binding energies of other species were calculated by introducing mutations to the interface according to the amino acid differences with Rosetta protein-protein ΔΔG protocol. Amino acid residues of ACE2 within 4.0Å of SARS-CoV-2 spike RBD were considered as interacting residues. Pymol was used to highlight the interacting sites in red in the ACE2 structure and to show the hydrogen bonds in yellow dash lines.

Virus and biosafety

SARS-CoV-2 was isolated from the nasopharyngeal aspirate specimen of a laboratory-confirmed COVID-19 patient in Hong Kong.[15] The plaque purified viral isolate was amplified by one additional passage in VeroE6 cells to make working stocks of the virus as described previously.[15] All experiments involving live SARS-CoV-2 followed the approved standard operating procedures of the HKU Biosafety Level-3 facility.

Animal model

Approval was obtained from the HKU Committee on the Use of Live Animals in Teaching and Research. Male and female Syrian hamsters, aged 6-10 weeks old, were obtained from HKU Laboratory Animal Unit. The animals were kept in Biosafety Level-2 housing and given access to standard pellet feed and water ad libitum until virus challenge in our Biosafety Level-3 animal facility. Phosphate-buffered saline(PBS) was used to dilute virus stocks to the desired concentration, and inocula were back-titrated to verify the dose given. Dulbecco's Modified Eagle Medium(DMEM) containing 10^5 plaque-forming units in 100μl of SARS-CoV-2 was intranasally inoculated under intraperitoneal ketamine(200mg/kg) and xylazine(10mg/kg)

anaesthesia. Mock-infected animals were challenged with 100ul of PBS. Animals were monitored twice daily for clinical signs of disease(Supplementary Figure S1). Their body weight and survival were monitored for 14 days post-inoculation(dpi). Five animals in each group were sacrificed at 2dpi, 4dpi, and 7dpi for virological and histolopathological analyses. Remaining animals were sacrificed at 14dpi. Blood and major organ tissues at necropsy were separated into two parts, one immediately fixed in 10% PBS-buffered formalin, the other immediately frozen at -80°C until use.

Histopathology, immunohistochemical, immunofluorescence, and TUNEL staining

These staining and microscopy procedures on tissue sections were performed as described previously with modifications(Supplementary Materials).[16]

Viral load and median tissue culture infectious dose ($TCID_{50}$) assays

Viral load studies by qRT-PCR assay were conducted on the blood and organ tissues. Quantitation of live infectious virus by $TCID_{50}$ assay was performed on the nasal turbinate and lung tissues(Supplementary Materials).[15]

Chemokine/cytokine profiling

Chemokine/cytokine profiling was performed on the lung tissues of the virus-challenged and mock-infected animals by qRT-PCR(Supplementary Materials and Table S1).[17]

Neutralising antibody detection and passive immunisation

Serum anti-SARS-CoV-2 neutralising antibody detection by microneutralisation assay and passive immunisation were performed as described previously(Supplementary Materials).[18,19]

Transmission study among close contact animals

Eight hamsters were intranasally challenged with SARS-CoV-2 (0dpi)(Supplementary Figure S2). Twenty-four hours later(1dpi), each SARS-CoV-2-challenged hamster was transferred to a new cage with each cage containing one naïve hamster as close contact. Five virus-challenged and five contact hamsters were sacrificed for viral load and histopathological studies at 4dpi and 4 days post-exposure, respectively. The remaining hamsters were kept for clinical observation until 14dpi. Surface spike gene of viral isolates from the hamsters was Sanger sequenced as described previously.[2]

Statistical analysis

All data were analysed with GraphPad Prism software(GraphPad Software,Inc). Weight losses were compared using two-way ANOVA and Student's t-test was used to determine significant differences in virus titres among the different groups.[16] $P<0.05$ was considered statistically significant.

Role of the funding source

The sponsors had no role in study design, data collection, analysis, interpretation, or writing of the report. The corresponding author had full access to all the data in the study and had final responsibility for the decision to submit for publication.

RESULTS

In silico prediction of animal species that might be susceptible to SARS-CoV-2

As the binding affinity of ACE2 to SARS-CoV-2 surface spike glycoprotein may be dictated by the amino acid composition at the binding interface, structural analysis was performed, which predicted 29 amino acid residues at the ACE2 interface that may interact with the SARS-CoV-2 spike glycoprotein RBD(Figure1A&1B). Comparison of the 29 amino acid residues' alignment between human and other mammalian species revealed that the rhesus macaque ACE2 is 100% identical to human ACE2 at the interface region. Syrian hamster and common marmoset ACE2 proteins are also highly similar to human ACE2, each with 3-4 mutations at the interface. The binding energy prediction using ACE2-SARS-CoV-2 spike RBD docking and protein-protein interface mutation ΔΔG modelling showed that the hamster ACE2 exhibited the highest binding affinity to the Spike of both SARS-CoV-2 [-49.96 Rosetta energy units(REU)] and SARS-CoV (-48.71REU) among all the species other than human and rhesus macaque(Supplementary Table S2). Notably, SARS-CoV-2 spike exhibited higher binding affinity with ACE2 than did SARS-CoV spike. This might be attributed to the more compact interacting interface with more hydrogen bonds formed between SARS-CoV-2 spike glycoprotein RBD and ACE2(Figure 1C). A Syrian hamster model was therefore evaluated to simulate the clinical, virological, pathological, and immunological manifestations of SARS-CoV-2-induced COVID-19.

Clinical features, tissue tropism, viral load, and virus titre changes

SARS-CoV-2-challenged but not mock-infected animals exhibited progressive mean body weight loss of up to ~11% from 1dpi-6dpi, then gradually regained their weight by 14dpi(Figure2A). They developed lethargy, ruffled furs, hunched back posture, and rapid

breathing since 2dpi and started to recover at 7dpi(Supplementary Videos V1&V2). None of the SARS-CoV-2-infected and mock-infected animals died.

To investigate the tissue tropism of SARS-CoV-2 in Syrian hamsters, we performed viral load studies on the upper respiratory tract(nasal turbinate), lower respiratory tract (trachea and lung), extrapulmonary organs(intestine, salivary glands, heart, liver, spleen, lymph nodes, kidney, and brain), and blood harvested from virus-challenged animals at different time points which represented the early(2dpi), severe(4dpi), and start of recovery(7dpi) phases. The mean viral loads(Figure2B) in the nasal turbinate and lung(10^2-10^3genome copies/β-actin), and trachea(10^1genome copies/β-actin) were consistently the highest among all tested organ tissues from 2dpi to 7dpi. The viral loads progressively decreased in airway tissues from 2dpi-7dpi. Viral culture of lung tissues showed high titre of 10^5-10^7 $TCID_{50}$/g at 2dpi&4dpi(Figure2C). As for extrapulmonary tissues, the mean viral load in the intestine was also highish especially on 4dpi. For other organ or blood, low mean viral loads(<1genome copy/β-actin) were detected at 2dpi and peaked at 4dpi, then progressively reduced to undetectable levels at 7dpi in most samples.

Histopathological changes in the respiratory tract

The nasal turbinate epithelium was intact with submucosal infiltration and blood vessel congestion at 2dpi(Figure3A). Abundant viral N protein expression was found throughout the epithelial layer and in some submucosal glands. At 4dpi, epithelial cell desquamation with viral N protein expression and increased intra-epithelial and submucosal infiltration were observed.

The trachea demonstrated epithelial cell swelling, focal cilia loss, and mononuclear cell infiltration into the epithelium and lamina propria at 2dpi(Figure3B). Desquamation of large

areas of the epithelium mixed with infiltrating mononuclear cells and cell debris was observed. Viral N protein was abundantly expressed in detached epithelial cells. TUNEL staining indicated severe apoptosis. At 4dpi, viral N protein was only associated with detached cell debris.

In the lungs, patches of focal inflammation and pleural invaginations were seen at 2dpi(Figure3C). Diffuse alveolar destruction, protein-rich fluid exudate, hyaline membrane formation, marked mononuclear cell infiltration, cell debris-filled bronchiolar lumen, and alveolar collapse with haemorrhage were observed. Viral N protein was abundantly expressed in bronchiolar epithelial cells, alveolar macrophages, and type I and II pneumocytes(Figure3D). TUNEL staining showed diffuse signals in the lung, bronchiolar lumen cell debris, and collapsed alveolar walls. At 4dpi, increasing lung consolidation and severe pulmonary haemorrhage were seen(Figure3E). Large syncytial bodies with multiple nuclei were seen in the epithelia of bronchioles and alveoli. Marked cellular proliferation with extensive expression of the proliferation marker Ki67 protein in both bronchiolar and alveolar cells was detected(Figure3F). More abundant viral N protein expression and TUNEL staining signals were found all over the alveolar wall(Figure3G).

At 7dpi, in the nasal turbinate mucosa, the intra-epithelial and submucosal infiltration persisted, but viral N protein expression in the epithelial layer was much reduced and mainly located in the cell debris(Figure4A). Tracheal epithelium recovered to an intact layer with cell proliferation forming projections into the lumen with scarce viral N protein expression. Very marked increase in pulmonary cellularity with the peaking of lung consolidation was seen(Figure4B). The mononuclear cell infiltrate and fluid exudate were now largely replaced by massive pneumocyte proliferation with intensified Ki67 expression. The proliferative changes involved the epithelia of the trachea, small bronchi, bronchioles, and alveoli. In the trachea and

small bronchi, the hyperplastic cells formed papillary projections into the lumen. The bronchioles and terminal bronchioles which are normally lined by simple cuboidal epithelium were replaced by multiple layers of irregularly arranged epithelial layers due to hyperplastic regeneration. Similarly, regenerative hyperplasia in the alveoli formed irregular-sized and -shaped structures. During this proliferative phase, viral N protein was no longer easily detectable. At 14dpi, only mild pulmonary congestion and inflammatory infiltration were still detectable (Figure4C). The air exchange structures were remodelled and restored to normal.

Histopathological changes in the extrapulmonary organ tissues

Though low levels of viral RNA were detected in multiple extrapulmonary organ tissues by qRT-PCR, viral N protein was only detected in the intestine (Figure5A). At 2dpi, intestinal mucosal epithelial cells were intact. The lamina propria exhibited more mononuclear cell infiltration. The Peyer's patches were enlarged without forming germinal centres. Few mucosal epithelial cells and interstitial histiocytes were weakly positive for viral N protein. At 4dpi, severe epithelial cell necrosis, damaged and deformed intestinal villi, and increased lamina propria mononuclear cell infiltration were observed. A large number of intestinal epithelial enterocytes were positive for viral N protein. The spleen size was markedly reduced at 2dpi&4dpi. Histopathology showed depletion of white and red pulps with reduced number and size of follicles(Figure5B). TUNEL staining showed increased apoptosis at 2dpi&4dpi. At 14dpi, increased follicular size and lymphocytes in red pulp were observed(Supplementary FigureS3A). The bronchial lymph nodes and mesenteric lymph nodes showed subcapsular and medullary lymphatic sinus ectasia with pale eosinophilic lymph(Supplementary FigureS3B). Viral N protein was not detected, but TUNEL-positive cells were abundantly found. The heart showed mild focal myocardial

degeneration and interstitial oedema at 2dpi&4dpi(Supplementary FigureS3C), but viral N protein was not detected. No histopathological changes were observed in other organs.

Chemokine/cytokine profile, neutralising antibody response, and passive immunisation

In line with the viral replication kinetics, the chemokine/cytokine profile in the lungs of the SARS-CoV-2-infected animals also exhibited a time-dependent trend of gene expression with triggering at 2dpi, peaking at 4dpi, and resolving at 7dpi(Supplementary FigureS4). Interferon-γ was potently induced at 2dpi, implying that SARS-CoV-2 triggered the innate immune response mediated by natural killer cells and T cells. Consistent with interferon-γ induction, pro-inflammatory chemokines/cytokines were induced and peaked at 4dpi, which represented the potent activation of inflammation and virus-induced cell-death. At 7dpi, type II interferon and pro-inflammatory cytokines such as interleukin-6 dropped to the basal level and increased TGF-β indicated the resolution of acute inflammation. Serum neutralising antibodies against SARS-CoV-2 were detected in challenged animals as early as 7dpi. The mean serum neutralising antibody titres at 7dpi&14dpi were ≥1:480 and ≥1:427 (1:160 to ≥1:640), respectively(Figure6A). Passive immunisation resulted in significantly reduced nasal turbinate and lung viral loads ($P<0.05$)(Figure6B), but there were no observable improvements in clinical signs and histopathological changes.

Transmission of SARS-CoV-2 among close contact animals

To study the transmissibility among close contacts, we housed SARS-CoV-2-challenged index hamsters and naïve contact hamsters in the same cage together in 1:1 ratio. The upper and lower respiratory tract specimens of both the index virus-challenged and naïve contact animals at 4

days after exposure were RT-PCR-positive for SARS-CoV-2 RNA(Figure6C). The mean viral loads in the respiratory tract tissues of the challenged animals were not significantly different. Interestingly, the index animals exhibited significantly more weight loss($P<0.05$) than the contact animals between 2dpi&8dpi(Figure6D). The histopathological changes and viral N protein expression in the contact animals' nasal turbinate, trachea, lung, and extrapulmonary tissues were similar to those of the challenged animals(Supplementary FigureS5). These findings confirmed that SARS-CoV-2 had spread by close contact from the challenged index animals to the naïve contact animals. Importantly, all contact hamsters were infected in this transmission study. Sequencing of the surface spike gene from the index and contact animals showed no changes except for one contact hamster with a H655Y mutation(Figure6E).

DISCUSSION

The clinical and histopathological findings from this SARS-CoV-2 hamster model closely resemble the manifestations of upper and lower respiratory tract infection in humans. The airway involvement is evident from nasal turbinate to trachea and pulmonary alveoli associated with changes of inflammation, cellular viral N protein expression, and high viral load during the first week. The disease progressed with increasing respiratory rate, decreasing activity, and progressive weight loss, and was most severe by 6dpi which is similar to the disease course of COVID-19 patients.[20] Histopathology showed progression from the initial phase of exudative inflammation to diffuse alveolar damage with haemorrhage and necrosis, and finally the proliferative phase after one week. Our findings were in agreement with the human autopsy findings except that our model also demonstrated extensive tissue apoptosis.[21] None of the challenged or contact hamsters died as <5% of human infections are lethal.[10]

As for extrapulmonary manifestations, though diarrhoea is not clinically evident in challenged hamsters, histopathology showed intestinal mucosal inflammation, epithelial necrosis and viral N protein expression in enterocytes. This finding corroborates with the clinical manifestation of diarrhoea in only 2.0%-10.1% of COVID-19 patients despite that up to 53% of their stool samples are RT-PCR positive.[7,22,23] Myocardial degenerative changes were noted both in our infected hamster and patient autopsy despite the absence of viral antigen detection in the tissues, which is also consistent with the occasional report of heart failure in COVID-19 patients.[22] Lymphoid atrophy and apoptosis in spleen were observed which correlate with the frequent clinical finding of lymphopenia(83.2%).[10] The lymphoid necrosis is largely related to the marked activation of innate immune response in infected hamsters with high levels of chemokines/cytokines induced by SARS-CoV-2 infection. Cytokine storm was observed in severe COVID-19, SARS, MERS, and influenza in human.[24-27] The mounting of adaptive immune response as evident by increasing titre of neutralising antibody was associated with the control of the viral load. Passive immunisation with early convalescent serum SARS-CoV-2 resulted in significantly lower viral loads in the respiratory tract without apparent differences in clinical signs and histopathological changes. Further studies with serum samples containing higher neutralising antibody titres should reveal the possible benefit or immunopathology associated with convalescent plasma therapy.[28]

Besides the satisfaction of the Koch's postulates by reproducing the clinical and pathological changes of pneumonia by virus challenge, recovery of pure virus from infected tissues, and detecting the rise of SARS-CoV-2-specific neutralising antibody, we also demonstrated virus transmission by close contact between the challenged index hamsters to the naïve contact hamsters housed in the same cages. It is notable that all five naïve contact animals

in five individual cages were infected. The minimal amount of weight loss in the naïve contact animals could be related to a lower virus inoculum when compared to the high single intranasal virus dose received by the challenged index animals. Though it was likely that the challenged animals were continuously shedding a high viral load in respiratory droplets which served as the most important portal of transmission, they might have also shed virus in their faeces as demonstrated by viral load study and N protein expression in the intestine. Hamsters are hindgut fermenters that eat their own faeces, a feeding behaviour called coprophagy, to recover nutrients digested in the hind-gut but unabsorbed.[29] Thus, faecal-oral route of transmission could not be excluded in this model as well as in human.

Readily available small animal models that resemble the clinical and pathological features of human COVID-19 are urgently needed to study pathogenesis, antiviral treatment, and vaccination. The external subdomain of the spike glycoprotein RBD of SARS-CoV-2 shares only 40% amino acid identity with SARS-CoV, but this new virus still utilizes ACE2 as the cell entry receptor which are abundantly found in epithelial linings of human and animals.[3,30] Our molecular docking and computation showed that the RBD of SARS-CoV-2 binds well with not only the ACE2 of human and macaques, but also with that of Syrian hamsters. Moreover, hamster was demonstrated to be a good model for studying respiratory viruses including SARS-CoV, influenza virus, and adenovirus.[31,32] Unlike our hamster model for SARS-CoV-2, it is also notable that weight loss or intestinal involvement were absent in the hamster model infected by the 2003 SARS-CoV.[31] More importantly, the viral load in the nasal turbinate(7-$\log_{10}$TCID$_{50}$/gram) of SARS-CoV-2-infected hamsters was consistently about ~1-log higher than that of their lung(~5.5-6-$\log_{10}$TCID$_{50}$/gram) at 2dpi, 4dpi, and 7dpi, whereas the viral load in the nasal turbinate of the 2003 SARS-CoV-infected hamsters were generally similar or lower than

that of the lung.[31] This might help to explain why SARS-CoV-2 is more transmissible as the upper respiratory tract involvement by the virus is no less than that of the lower respiratory tract, whereas SARS-CoV predominantly infects the lower respiratory tract.

Our study had a number of limitations. First, the virus inocula used in this study and the previous report of 2003 SARS-CoV hamster model were different, which might contribute to the differences in findings. Second, we tested the mRNA but not protein expression of the hamsters' chemokine/cytokine profiles as enzyme-immunoassay for hamster chemokines/cytokines were unavailable. Finally, we focused our sequencing on the surface spike gene which is essential for virus-host cell entry. Complete genome sequencing may reveal additional adaptive mutations in other genome regions. Nevertheless, unlike non-human primates and ACE2-transgenic mice, this hamster model is readily available, physiological, and highly resembles COVID-19. Thus, it would be an important platform for studying the pathogenesis, transmission, treatments, and vaccines for COVID-19.

Notes

Author contributions. JF-WC, AJZ, SY, and K-YY had roles in the study design, data collection, data analysis, data interpretation, and writing of the manuscript. VK-MP and CC-SC had roles in the study design, experiments, data collection, data analysis, and data interpretation. AC-YL, W-MC, ZF, H-WT, LW, RL, JC, YC, KT, CL, J-PC, K-HK, HChu, K-HC, SS, ZC, HChe, and KK-WT had roles in the experiments, data collection, data analysis, and/or data interpretation. All authors reviewed and approved the final version of the manuscript.

Acknowledgements and financial support. This study was partly supported by the donations of May Tam Mak Mei Yin, Richard Yu and Carol Yu, Michael Seak-Kan Tong, the Shaw Foundation Hong Kong, Respiratory Viral Research Foundation Limited, Hui Ming, Hui Hoy and Chow Sin Lan Charity Fund Limited, Chan Yin Chuen Memorial Charitable Foundation, Marina Man-Wai Lee, the Hong Kong Hainan Commercial Association South China Microbiology Research Fund, and the Jessie & George Ho Charitable Foundation; and funding from the Consultancy Service for Enhancing Laboratory Surveillance of Emerging Infectious Diseases and Research Capability on Antimicrobial Resistance for Department of Health of the Hong Kong Special Administrative Region Government; the Theme-Based Research Scheme (T11/707/15) of the Research Grants Council, Hong Kong Special Administrative Region; Sanming Project of Medicine in Shenzhen, China (No. SZSM201911014); and the High Level-Hospital Program, Health Commission of Guangdong Province, China. The funding sources had no role in the study design, data collection, analysis, interpretation, or writing of the report.

Potential conflicts of interests. We declare no competing interests.

References

1. Zhu N, Zhang D, Wang W, et al. A Novel Coronavirus from Patients with Pneumonia in China, 2019. *N Engl J Med* 2020;382:727-733.

2. Chan JF, Yuan S, Kok KH, et al. A familial cluster of pneumonia associated with the 2019 novel coronavirus indicating person-to-person transmission: a study of a family cluster. *Lancet* 2020;395(10223):514-523.

3. Chan JF, Kok KH, Zhu Z, et al. Genomic characterization of the 2019 novel human-pathogenic coronavirus isolated from a patient with atypical pneumonia after visiting Wuhan. *Emerg Microbes Infect* 2020; **9**(1): 221-236.

4. Channel News Asia. South Korea's coronavirus cases climb above 7,000, most cases traced to church. March 7, 2020. https://www.channelnewsasia.com/news/asia/south-korea-s-coronavirus-cases-climb-above-7-000-most-cases-12512784 (accessed on March 9, 2020)

5. Rocklov J, Sjodin H, Wilder-Smith A. COVID-19 outbreak on the Diamond Princess cruise ship: estimating the epidemic potential and effectiveness of public health countermeasures. *J Travel Med* 2020; Feb 28. pii: taaa030. doi: 10.1093/jtm/taaa030. [Epub ahead of print]

6. Kamp J. The Wall Street Journal: Coronavirus Spreads to More Elder Facilities in Seattle Area. March 10, 2020. https://www.wsj.com/articles/coronavirus-spreads-to-more-elder-facilities-in-seattle-area-11583884557 (accessed on March 10, 2020)

7. Wang D, Hu B, Hu C, et al. Clinical Characteristics of 138 Hospitalized Patients With 2019 Novel Coronavirus-Infected Pneumonia in Wuhan, China. *JAMA* 2020.

8. World Health Organisation. Coroanvirus disease (COVID-2019) situation report – 49. March 9, 2020. https://www.who.int/docs/default-source/coronaviruse/situation-reports/20200309-sitrep-49-covid-19.pdf?sfvrsn=70dabe61_4 (accessed on March 9, 2020)

9. Wei M, Yuan J, Liu Y, Fu T, Yu X, Zhang ZJ. Novel Coronavirus Infection in Hospitalized Infants Under 1 Year of Age in China. *JAMA* 2020; Feb 14. doi: 10.1001/jama.2020.2131. [Epub ahead of print]

10. Guan WJ, Ni ZY, Hu Y, et al. Clinical Characteristics of Coronavirus Disease 2019 in China. *N Engl J Med* 2020; Feb 28. doi: 10.1056/NEJMoa2002032. [Epub ahead of print]

11. Callaway E. How monkeys, mice and ferrets are helping scientists to fight coronavirus. March 9, 2020. *Nature*. https://www.nature.com/articles/d41586-020-00698-x (accessed on March 9, 2020)

12. Edgar RC. MUSCLE: multiple sequence alignment with high accuracy and high throughput. *Nucleic Acids Res* 2004; **32**(5): 1792-1797.

13. Zhang Y. I-TASSER server for protein 3D structure prediction. *BMC Bioinformatics* 2008; **9**: 40.

14. Das R, Baker D. Macromolecular modeling with rosetta. *Annu Rev Biochem* 2008; **77**: 363-382.

15. Chan JF, Yip CC, To KK, et al. Improved molecular diagnosis of COVID-19 by the novel, highly sensitive and specific COVID-19-RdRp/Hel real-time reverse transcription-polymerase chain reaction assay validated in vitro and with clinical specimens. *J Clin Microbiol* 2020; Mar 4. pii: JCM.00310-20. doi: 10.1128/JCM.00310-20. [Epub ahead of print]

16. Chan JF, Zhang AJ, Chan CC, et al. Zika Virus Infection in Dexamethasone-immunosuppressed Mice Demonstrating Disseminated Infection with Multi-organ Involvement Including Orchitis Effectively Treated by Recombinant Type I Interferons. *EBioMedicine* 2016; **14**: 112-22.

17. Espitia CM, Zhao W, Saldarriaga O, et al. Duplex real-time reverse transcriptase PCR to determine cytokine mRNA expression in a hamster model of New World cutaneous leishmaniasis. *BMC Immunol* 2010; **11**: 31.

18. To KK, Tsang OT, Leung WS, et al. Temporal profiles of deep throat saliva viral load and serum antibody response during COVID-19 infection by SARS-CoV-2: an observational cohort study. *Lancet Infect Dis* 2020. (accepted and in press)

19. Julander JG, Testori M, Cheminay C, Volkmann A. Immunogenicity and Protection After Vaccination With a Modified Vaccinia Virus Ankara-Vectored Yellow Fever Vaccine in the Hamster Model. *Front Immunol* 2018; **9**: 1756.

20. Huang C, Wang Y, Li X, et al. Clinical features of patients infected with 2019 novel coronavirus in Wuhan, China. *Lancet* 2020; **395**: 497-506.

21. Xu Z, Shi L, Wang Y, et al. Pathological findings of COVID-19 associated with acute respiratory distress syndrome. *Lancet Respir Med* 2020; Feb 18. pii: S2213-2600(20)30076-X. doi: 10.1016/S2213-2600(20)30076-X. [Epub ahead of print]

22. Chen N, Zhou M, Dong X, et al. Epidemiological and clinical characteristics of 99 cases of 2019 novel coronavirus pneumonia in Wuhan, China: a descriptive study. *Lancet* 2020; **395**(10223): 507-513.

23. Pan Y, Zhang D, Yang P, Poon LLM, Wang Q. Viral load of SARS-CoV-2 in clinical samples. *Lancet Infect Dis* 2020; Feb 24. pii: S1473-3099(20)30113-4. doi: 10.1016/S1473-3099(20)30113-4. [Epub ahead of print]

24. Ruan Q, Yang K, Wang W, Jiang L, Song J. Clinical predictors of mortality due to COVID-19 based on an analysis of data of 150 patients from Wuhan, China. *Intensive Care Med* 2020 Mar 3. doi: 10.1007/s00134-020-05991-x. [Epub ahead of print]

25. Cheng VC, Lau SK, Woo PC, Yuen KY. Severe acute respiratory syndrome coronavirus as an agent of emerging and reemerging infection. *Clin Microbiol Rev* 2007; **20**:660-94.

26. Chan JF, Lau SK, To KK, Cheng VC, Woo PC, Yuen KY. Middle East respiratory syndrome coronavirus: another zoonotic betacoronavirus causing SARS-like disease. *Clin Microbiol Rev* 2015; **28**: 465-522.

27. Cheng VC, To KK, Tse H, Hung IF, Yuen KY. Two years after pandemic influenza A/2009/H1N1: what have we learned? *Clin Microbiol Rev* 2012; **25**: 223-263.

28. Liu L, Wei Q, Lin Q, et al. Anti-spike IgG causes severe acute lung injury by skewing macrophage responses during acute SARS-CoV infection. *JCI Insight* 2019;**4**.

29. Grant K. Rodent nutrition: digestive comparisons of 4 common rodent species. *Vet Clin North Am Exot Anim Pract* 2014; **17**: 471-483.

30. Zhou P, Yang XL, Wang XG, et al. A pneumonia outbreak associated with a new coronavirus of probable bat origin. *Nature* 2020; Feb 3. doi: 10.1038/s41586-020-2012-7. [Epub ahead of print]

31. Roberts A, Vogel L, Guarner J, et al. Severe acute respiratory syndrome coronavirus infection of golden Syrian hamsters. *J Virol* 2005; **79**: 503-511.

32. Miao J, Chard LS, Wang Z, Wang Y. Syrian Hamster as an Animal Model for the Study on Infectious Diseases. *Front Immunol* 2019; **10**: 2329.

Figure legends

Figure 1. Interaction between the SARS-CoV-2 spike glycoprotein receptor-binding domain (RBD) and angiotensin-converting enzyme 2 (ACE2).

(A) Multiple alignment of the amino acid residues from ACE2 proteins of human and other mammalian species. The dots indicate amino acid residues that are identical between the human and mammalian ACE2.

(B) Interaction model of the SARS-CoV-2 spike glycoprotein S1 subunit RBD (magenta) and human ACE2 (grey) in front (left), side (middle), and back (right) views. The ACE2 amino acid residues within 4.0Å of the SARS-CoV-2 spike glycoprotein S1 subunit RBD are highlighted in red.

(C) Hydrogen bonds between ACE2 and the spike glycoprotein S1 subunit RBDs of SARS-CoV-2 (left) and SARS-CoV (right). Hydrogen bonds are indicated by yellow dashed lines and hydrogen bond donors and acceptors are represented by sticks (oxygen = red sticks; nitrogen = blue sticks; carbon = green sticks in ACE2 and grey sticks in RBDs).

Figure 2. Body weight changes and tissue tropism of SARS-CoV-2 infection in the Syrian hamster model.

(A) Body weight changes of SARS-CoV-2-challenged (n=11 at 0dpi to 7dpi; n=6 at 8dpi to 14dpi as 5 animals were sacrificed) and mock-infected (n=3 at 0dpi to 14dpi) hamsters.

(B) Viral load by qRT-PCR assay in the respiratory tract tissues, extrapulmonary organ tissues, and blood of SARS-CoV-2-challenged hamsters at 2dpi, 4dpi, and 7dpi (n=3 per day).

(C) Quantitation of virus titre by $TCID_{50}$ assay in the nasal turbinate and lung of SARS-CoV-2-challenged hamsters at 2dpi, 4dpi, and 7dpi (n=5 per day).

* denotes P<0.05, ** denotes P<0.01, *** denotes P<0.0001 by two-way ANOVA. Error bars represent standard deviations of the mean.

Figure 3. Histopathological, immunohistochemical, immunofluorescence, and TUNEL staining findings of respiratory tract tissues at days 2 and 4 after SARS-CoV-2 infection.

(A) Images of H&E and immunofluorescence stained nasal turbinate sections at 2dpi and 4dpi. (a) At 2dpi, the epithelial layer was relatively intact with submucosal infiltration. (b) SARS-CoV-2 N protein (green) was present almost throughout the entire epithelial layer and in some submucosal glands (insert). Cell nuclei were stained by DAPI (blue). (c) At 4dpi, epithelial cell death and desquamation was mild, but the intra-epithelial and submucosal infiltration increased. (d) Viral N protein was expressed in the epithelial cells and cell debris.

(B) Trachea. (a) at 2dpi, epithelial desquamation and loss of mucosal integrity with plugs of cell debris in the tracheal lumen were observed (black arrows) along with lamina propria connective tissue infiltration. The black square area was magnified showing detached epithelial cells mixed with mononuclear cells (short arrows); (b) Viral N protein (white arrows and magnified images) was mostly found in intraluminal cell debris. (c) The same section of trachea was positive by terminal deoxynucleotidyl transferase dUTP nick end labelling (TUNEL) staining (green) indicating apoptotic cell death. At 4dpi, (d) tracheal epithelial desquamation and submucosal infiltration is mild and (e) viral N protein was only found in intraluminal cell debris.

(C) Histopathological changes in the lungs at 2dpi. At low magnification (4×), patches of focal inflammation with intense colour and pleural invaginations (arrows) were seen. (a & b) Varying severities of diffuse lung damage, including (c) protein-rich exudates and hyaline membrane filled alveolar space; (d) large amount of mononuclear cells infiltrating alveolar sac; (e) cell

debris in bronchiolar lumen (arrows); and (f) alveolar collapse with cell death and acute haemorrhage (arrows).

(D) Viral N protein expression and TUNEL staining in the lungs. (a) SARS-CoV2 N protein distribution in the lung ("B" = bronchiole; "A" = alveoli; "V" = blood vessel). (b) and (c) are magnified images illustrating viral N protein-positive staining in alveolar macrophages (thin arrows in a and b), type I (arrow heads in c) and type II pneumocytes (thick arrows in b). (d) to (f) showing TUNEL labelling in the lung tissues of representative fields.

(E) Histopathological changes of the lungs at 4dpi. (a) and (b) Low magnification scanning (4×) showing diffuse inflammation, large areas of consolidation, pleural invaginations (thin arrows), and severe haemorrhage (thick arrows). (c) Representative images of patchy consolidation and (d) pulmonary haemorrhage. High magnification showing (e) intense peribronchiolar infiltration, epithelial cells swelling, intra-epithelial layer infiltration, mixture of cell debris and exudates filling in the bronchiolar lumen and a gigantic multinucleated syncytial body in the magnified image (arrows); (f) and (g) various sizes and locations of syncytial bodies (arrows); (h) alveolar collapse with mononuclear cell infiltrate and dead epithelial cells in alveolar space (arrows); and (i) marked haemorrhagic exudates with tissue destruction.

(F) Extensive pulmonary cellular proliferation forming multiple layers of thickened alveolar wall. Immunohistochemical staining showed extensive expression of proliferation marker Ki67 in bronchiolar epithelium and alveoli.

(G) Diffuse distribution of viral N protein and TUNEL staining showed diffuse apoptotic cell death in the lungs.

Figure 4. Histopathological changes of upper and lower respiratory tract tissues at days 7 and 14 after SARS-CoV-2 infection.

(A) At 7dpi, nasal turbinate tissue (left panel) showed mild submucosal infiltration. The epithelium was intact with a few mononuclear cells and cell debris seen in the luminal side. Viral N protein was only seen in the debris. Tracheal epithelial layer (right panel) was restored with cell proliferation forming projections into the lumen. No viral N protein expression was detected.

(B) Lung sections showed consolidation involving nearly half of the cutting area. (a) Lung consolidation around two bronchi and pulmonary blood vessel; (b) proliferative bronchiolar epithelial and alveolar cells; (c) proliferation of alveolar cells formed granular structures which were (d) stained strongly positive by Ki67 antibody; epithelial cell proliferation and hyperplasia in (e) trachea and (f) small bronchi with the hyperplastic cells forming papillary projections into the lumen (arrows); (g) bronchioles and terminal bronchioles, and (h) alveoli showing irregular-sized and -shaped hyperplastic cells (arrows).

(C) Histopathological changes of the lung at 14dpi. The lungs showed mild blood vessel congestion and mononuclear cell infiltration, bronchiolar and alveolar epithelium proliferation, and restored tissue structures with largely resolved inflammation.

Figure 5. Representative histopathological changes of intestine and spleen of SARS-CoV-2-challenged hamsters.

(A) H&E and immunofluorescence staining of intestinal tissue at 2dpi. (a) Mock-infected hamster intestine; (b) and (c) intestinal mucosal epithelia and Peyer's patches of virus-challenged hamsters at 2dpi; (d) a few mucosal epithelial cells and interstitial histiocytes were found weakly

positive for viral N protein (arrows); (e) epithelial cell necrosis and (f) viral N protein expression (arrows) in the intestine at 4dpi.

(B) Images of H&E- and TUNEL-stained spleen sections at 2dpi and 4dpi.

Figure 6. Application of the hamster model for studying the effects of immunoprophylaxis and transmission of SARS-CoV-2.

Passive immunisation study: **(A) Reciprocal serum SARS-CoV-2-specific neutralising antibody titres** in SARS-CoV-2-infected hamsters on the indicated days following intranasal challenge. The mean antibody titres from three hamsters per group are shown on a logarithmic scale. The dotted line indicates the lower limit of detection (<1:20). **(B) Viral load in the nasal turbinate and lung tissues** of the hamsters that received SARS-CoV-2-infected hamster convalescent serum collected at 14dpi (n=5) and those that received mock-infected hamster convalescent serum (n=3). Error bars represent standard deviations of the mean. Student's t-test was used to calculate statistical significance.

Transmission study of SARS-CoV-2 among close contact hamsters: **(C) Viral load by qRT-PCR assay** in the respiratory tract tissues of SARS-CoV-2-challenged and naïve contact hamsters at 4dpi and 4 days after exposure, respectively (n=5 per group). **(D) Body weight changes** of SARS-CoV-2-challenged index (n=8 at 0dpi to 4dpi; n=3 at 5dpi to 14dpi as 5 animals were sacrificed at 4dpi) and naïve contact (n=8 at 0dpi to 4dpi; n=3 at 5dpi to 14dpi) hamsters. **(E) Amino acid substitution in spike-coding sequences.** Samples obtained from the SARS-CoV-2-challenged index hamsters and naïve contact hamsters were subjected to Sanger sequencing. Spike-coding sequences of each sample were compared and the positions corresponding to the spike gene were listed. The nucleotide substitutions were underlined.

* denotes P<0.05, ** denotes P<0.01, *** denotes P<0.0001 by two-way ANOVA. Error bars represent standard deviations of the mean.

Abbreviations: FP, fusion peptide; HR1, heptad repeat 1; HR2, heptad repeat 1 and 2; NTD, N-terminal domain; RBD, receptor-binding domain; S1, Spike S1 subunit; S2, Spike S2 subunit; SP, signal peptide; TM, Transmembrane domain.

Figure 1

A

Species	Sequence variation of ACE2 residues interacting with SARS-CoV-2 spike RBD																											
	19	23	24	26	27	28	30	31	34	38	41	76	79	82	83	84	324	325	326	329	330	353	354	355	357	383	386	387	393
Homo sapiens (Human)	S	E	Q	K	T	F	D	K	H	D	Y	Q	L	M	Y	P	T	Q	G	E	N	K	G	D	R	M	A	A	R
Macaca mulatta (Rhesus macaque)	.	.	.	.	.	.	.	.	.	.	.	.	.	.	.	.	.	.	.	.	.	.	.	.	.	.	.	.	.
Callithrix jacchus (Common marmoset)	.	.	.	.	.	.	.	.	.	.	H	.	.	T	.	.	.	.	.	.	.	.	Q	.	.	.	.	.	.
Mesocricetus auratus (Hamster)	.	.	.	.	.	.	.	.	Q	.	.	.	.	N	.	S	.	.	.	.	.	.	.	.	.	.	.	T	.
Oryctolagus cuniculus (Rabbit)	.	.	L	.	.	.	E	.	Q	.	.	.	.	T	.	.	.	.	.	.	.	.	.	.	.	.	.	T	.
Mustela putorius furo (Ferret)	.	D	L	.	.	.	E	.	Y	E	.	E	H	T	.	.	.	E	.	Q	.	.	R	.	.	.	.	E	.
Rattus norvegicus (Rat)	.	.	K	E	S	.	N	.	Q	.	.	.	I	N	F	S	.	P	.	T	.	H	.	.	.	.	.	K	.
Mus musculus (Mouse)	.	.	N	.	.	.	N	N	Q	.	.	.	T	S	F	S	.	.	.	A	.	H	.	.	.	.	.	R	.
Sus scrofa (Pig)	.	.	L	.	.	.	E	.	L	.	.	.	I	T	.	.	.	.	.	N	.	.	.	.	.	.	.	I	.
Rhinolophus sinicus (Bat)	.	D	R	.	.	.	.	E	S	N	.	.	.	N	.	.	.	E	.	N	.	.	.	.	.	.	.	S	.

B

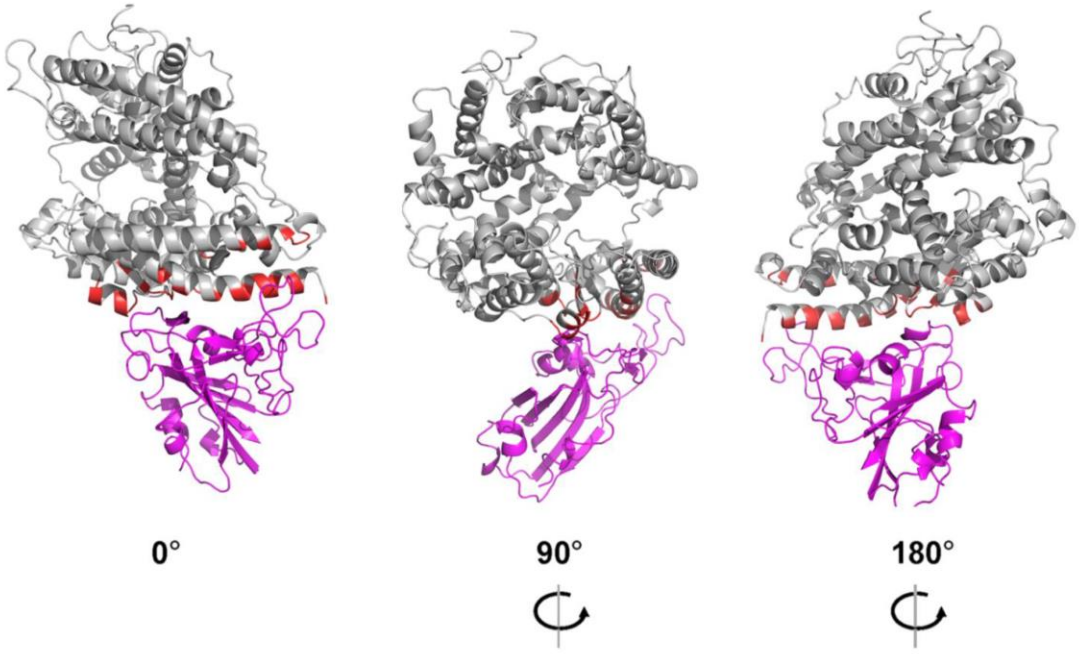

C

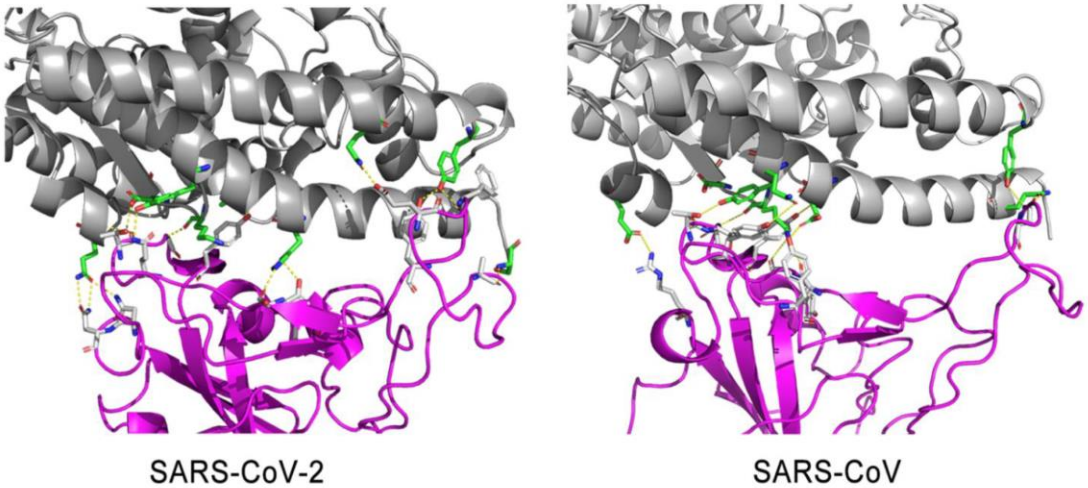

Figure 2A

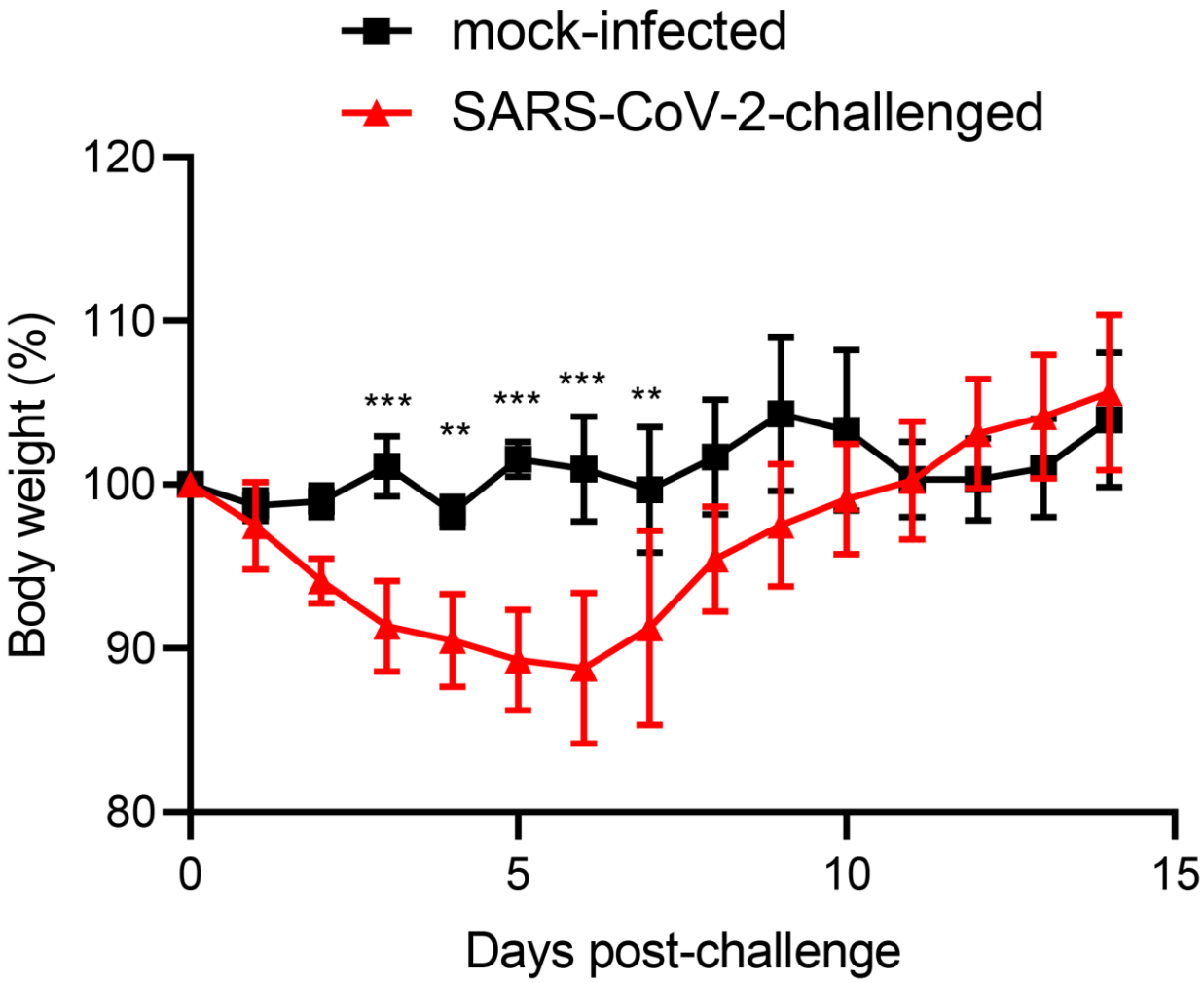

Figure 2B

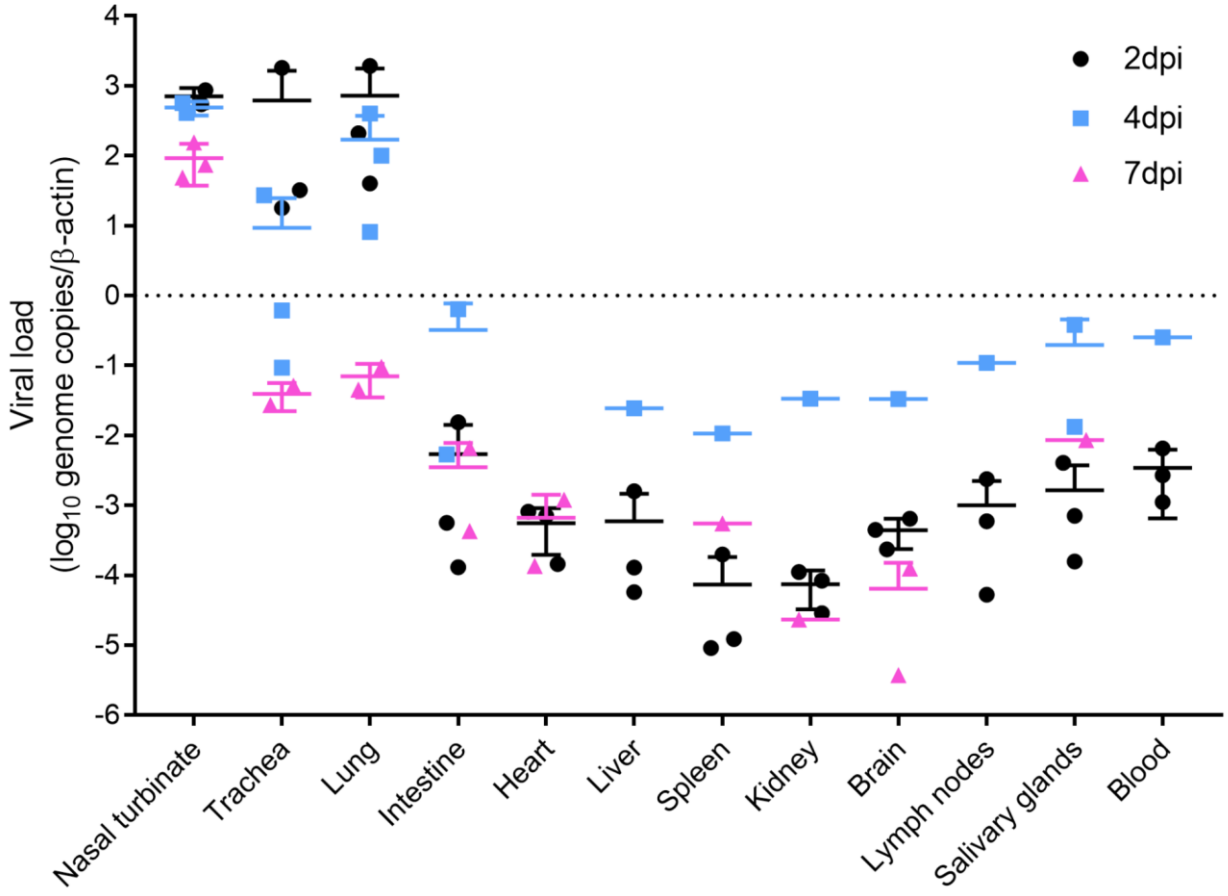

Figure 2C

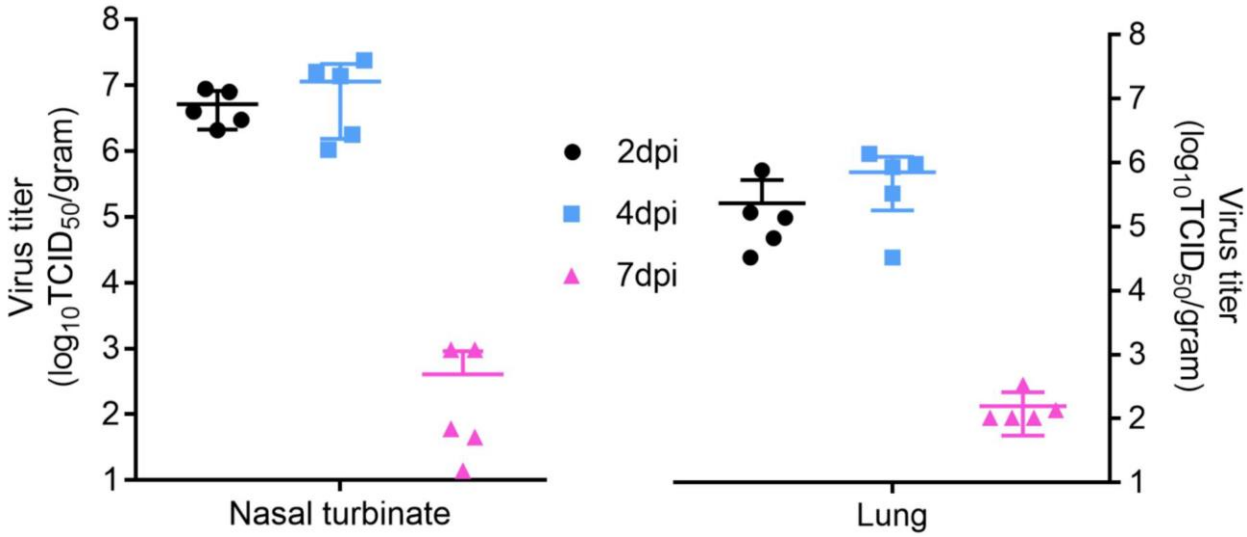

Figure 3A

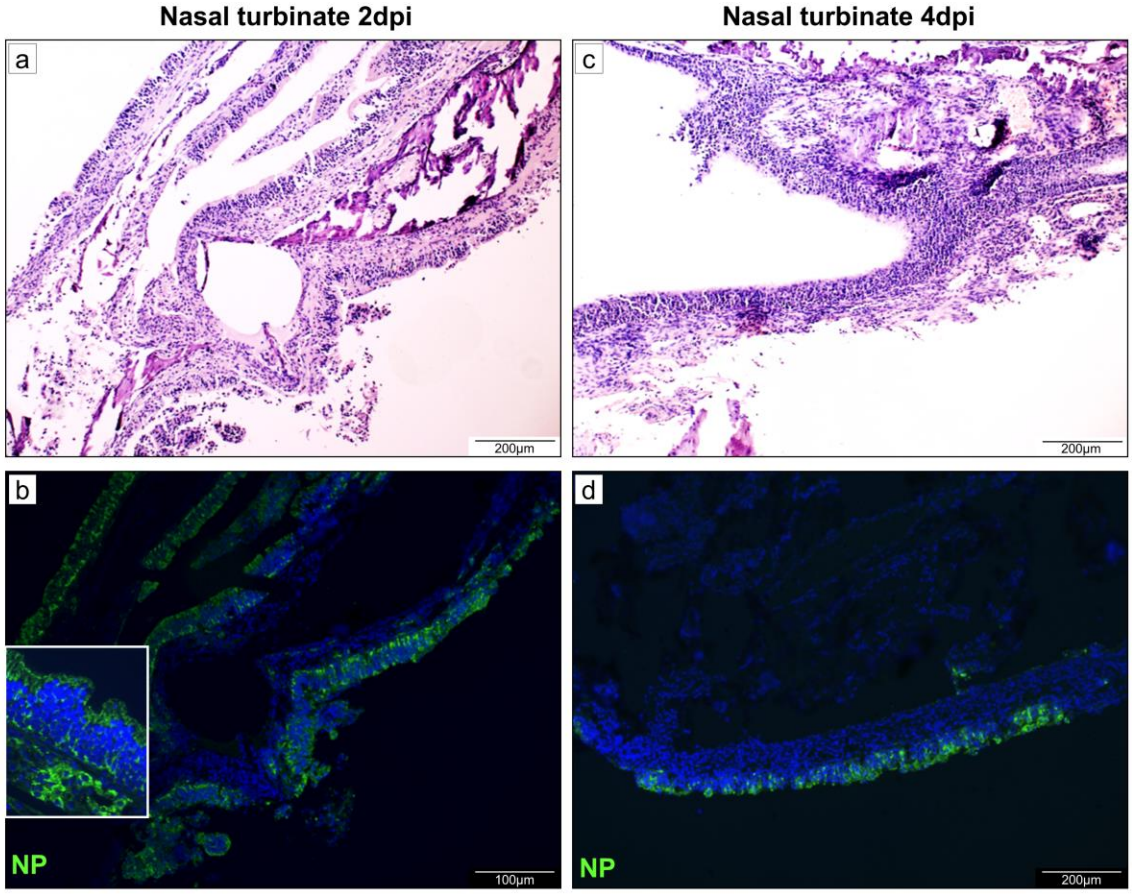

Figure 3B

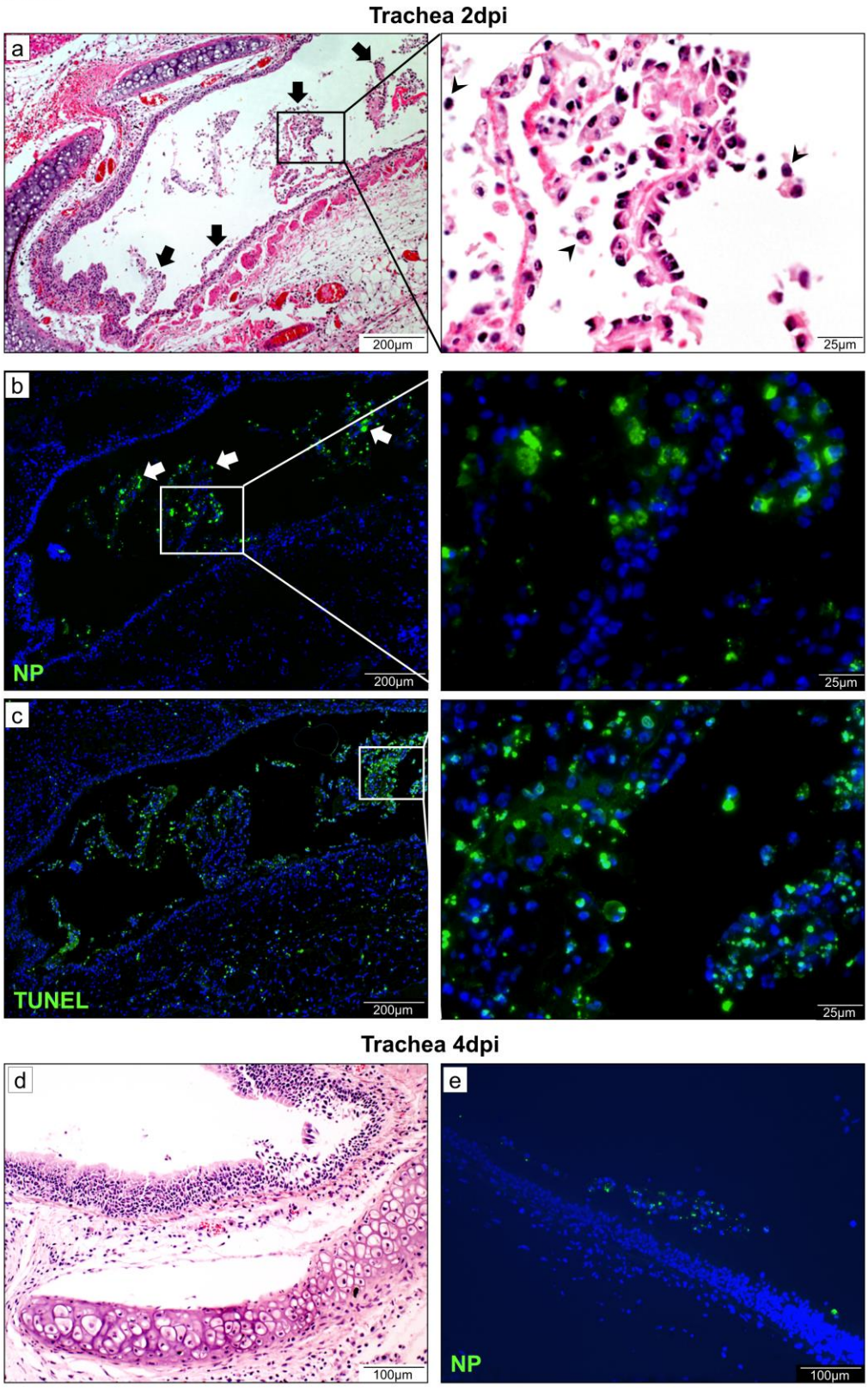

Figure 3C

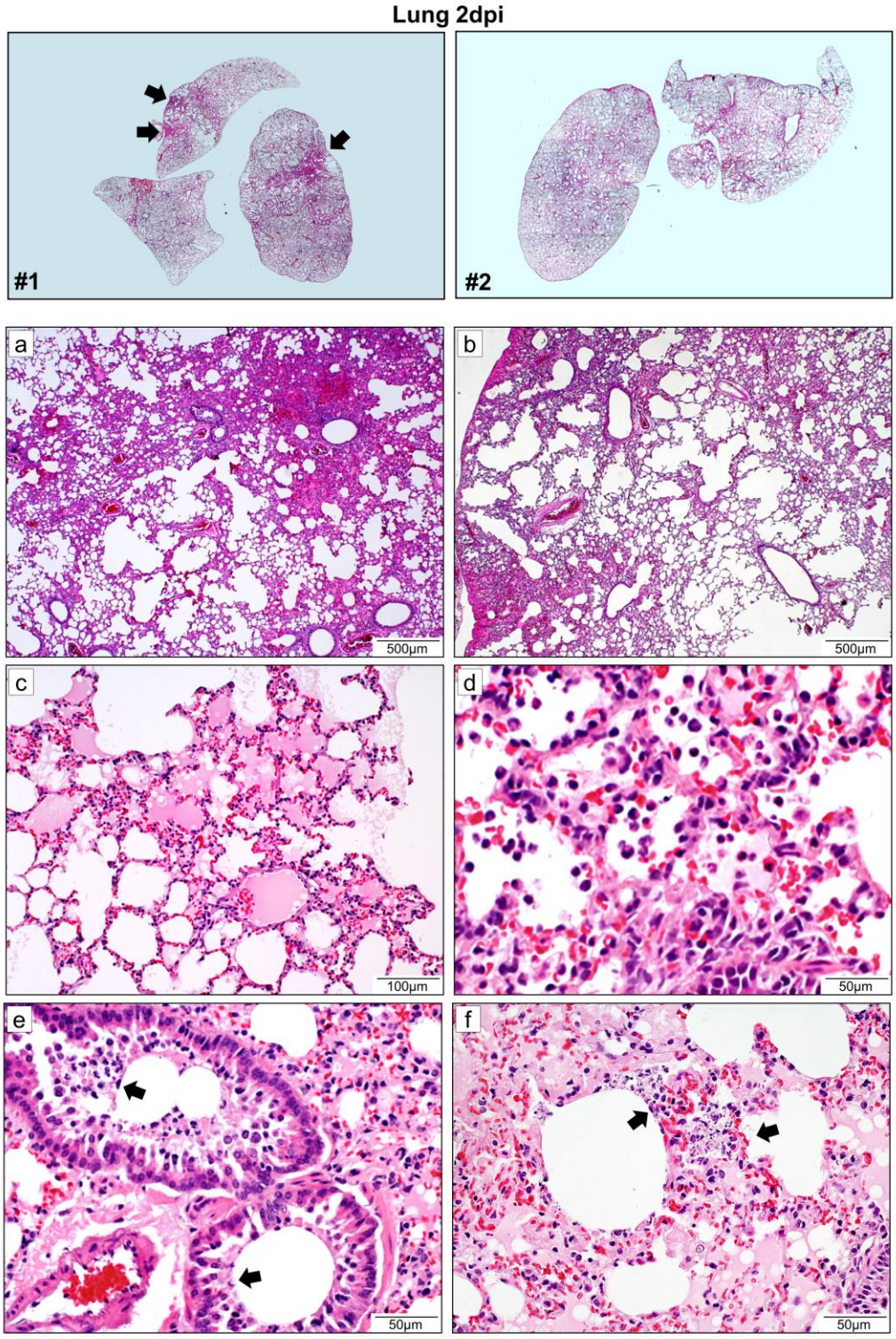

Figure 3D

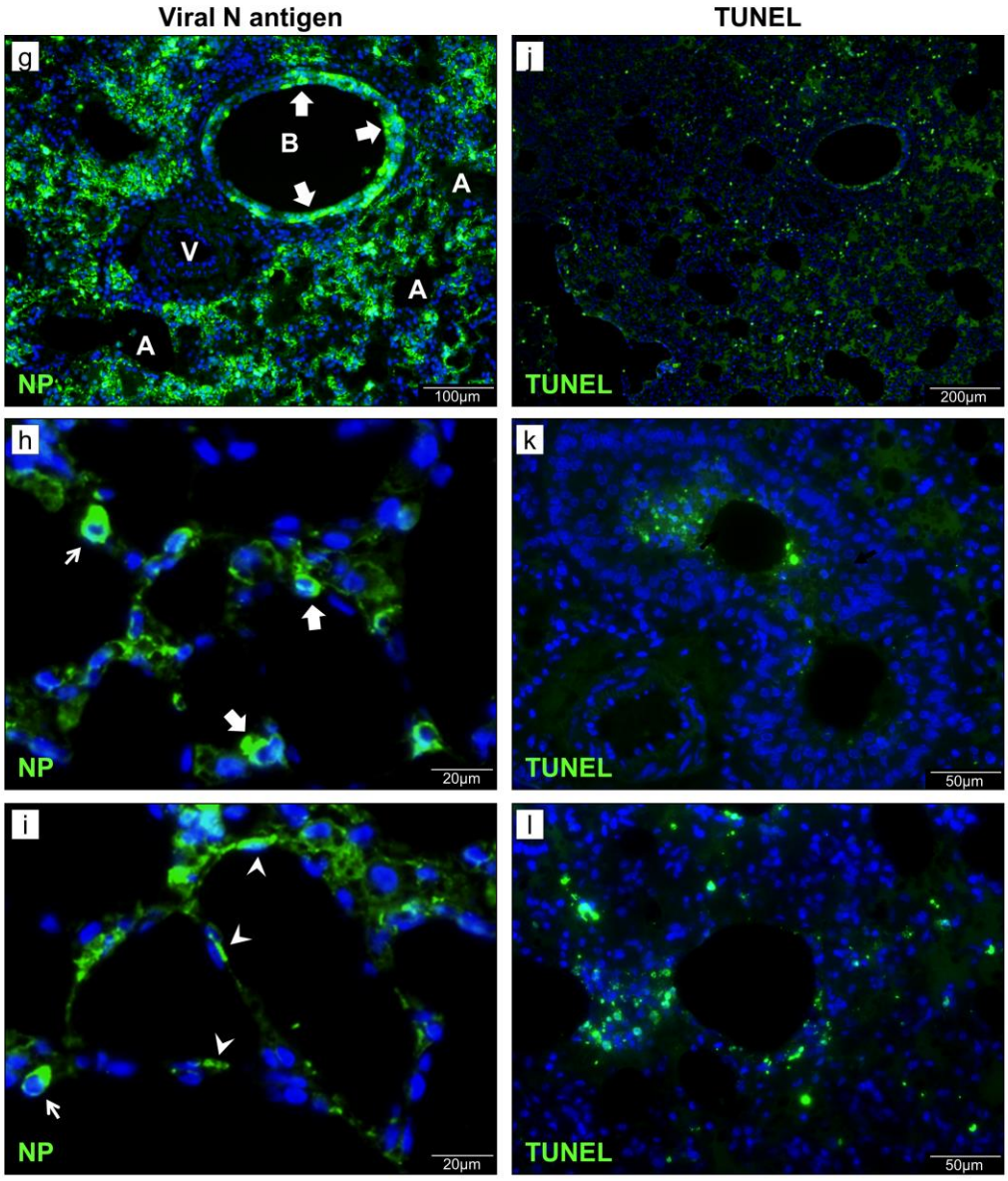

Figure 3E

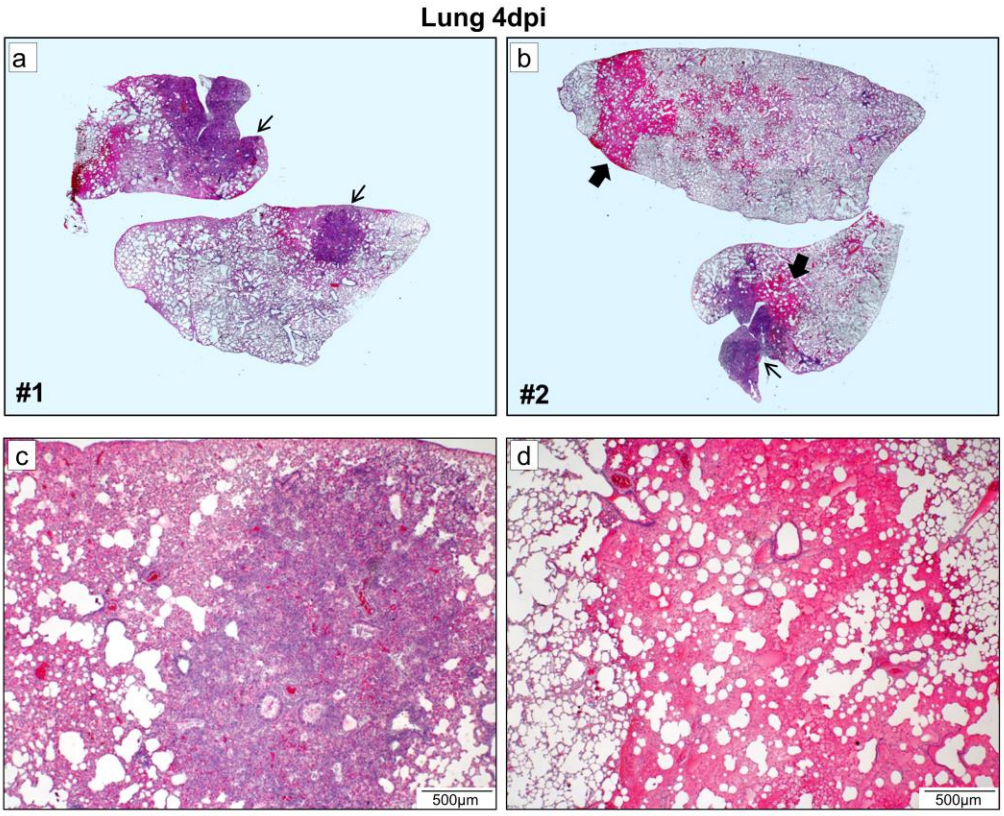

Figure 3E

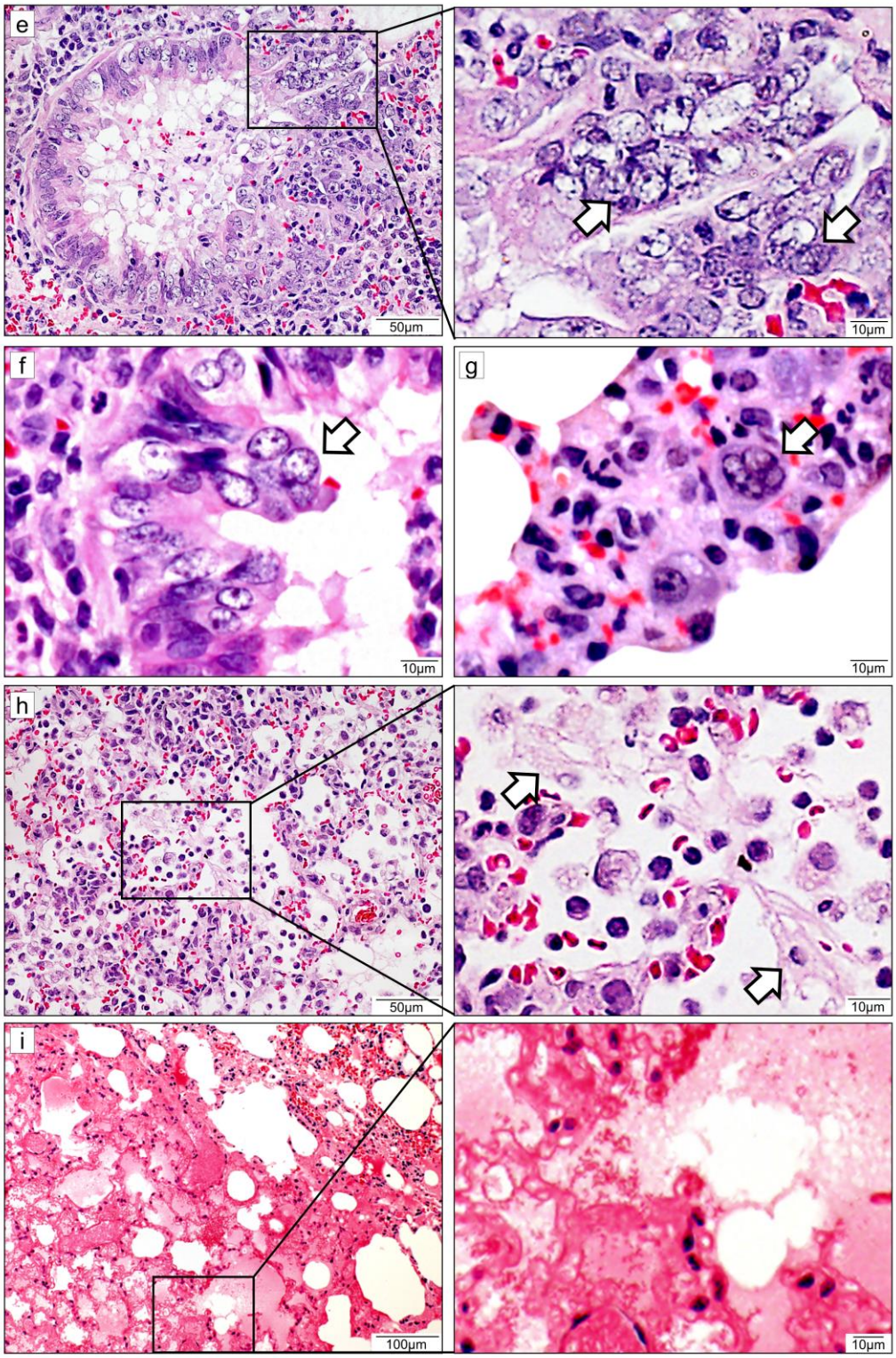

Figure 3F

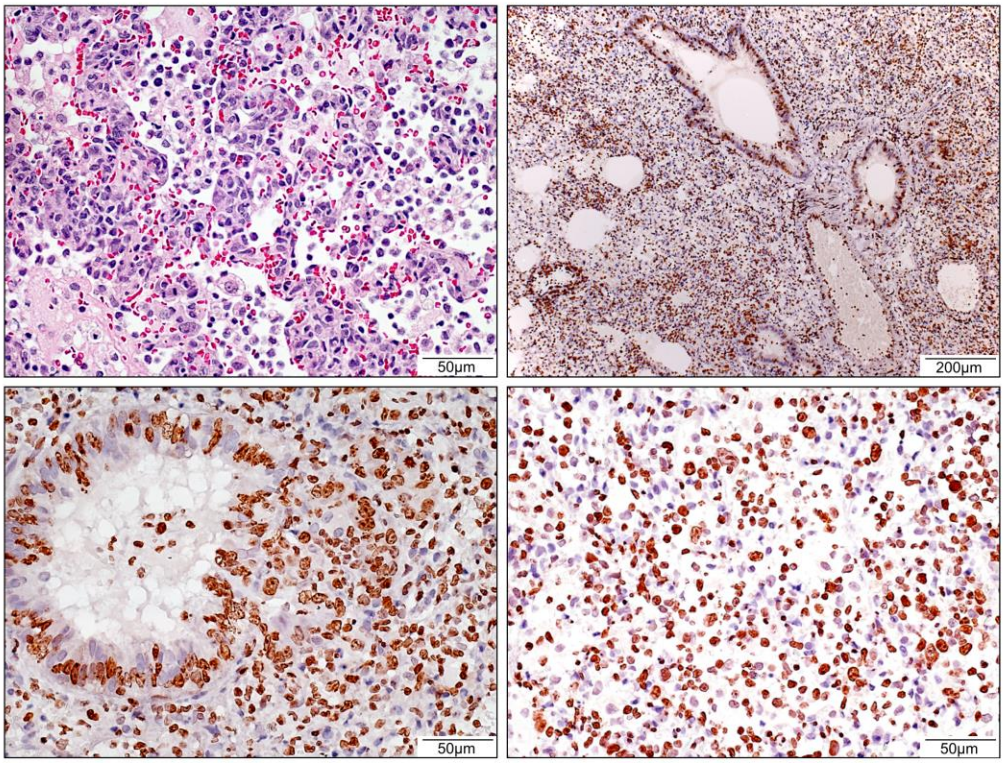

Figure 3G

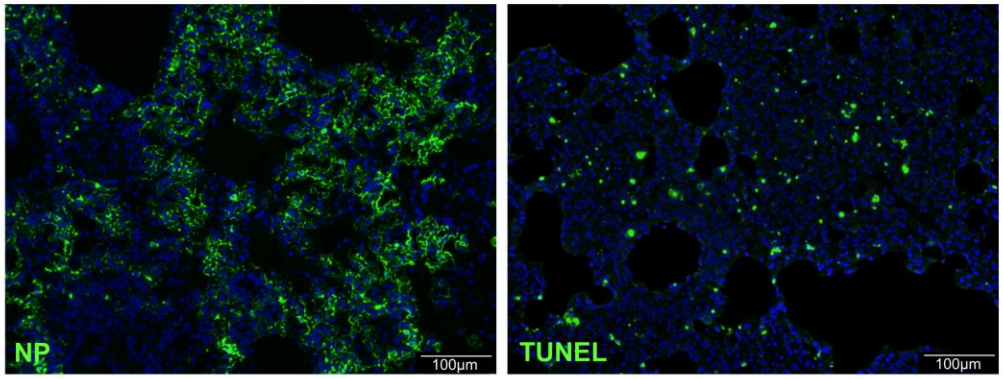

Figure 4A

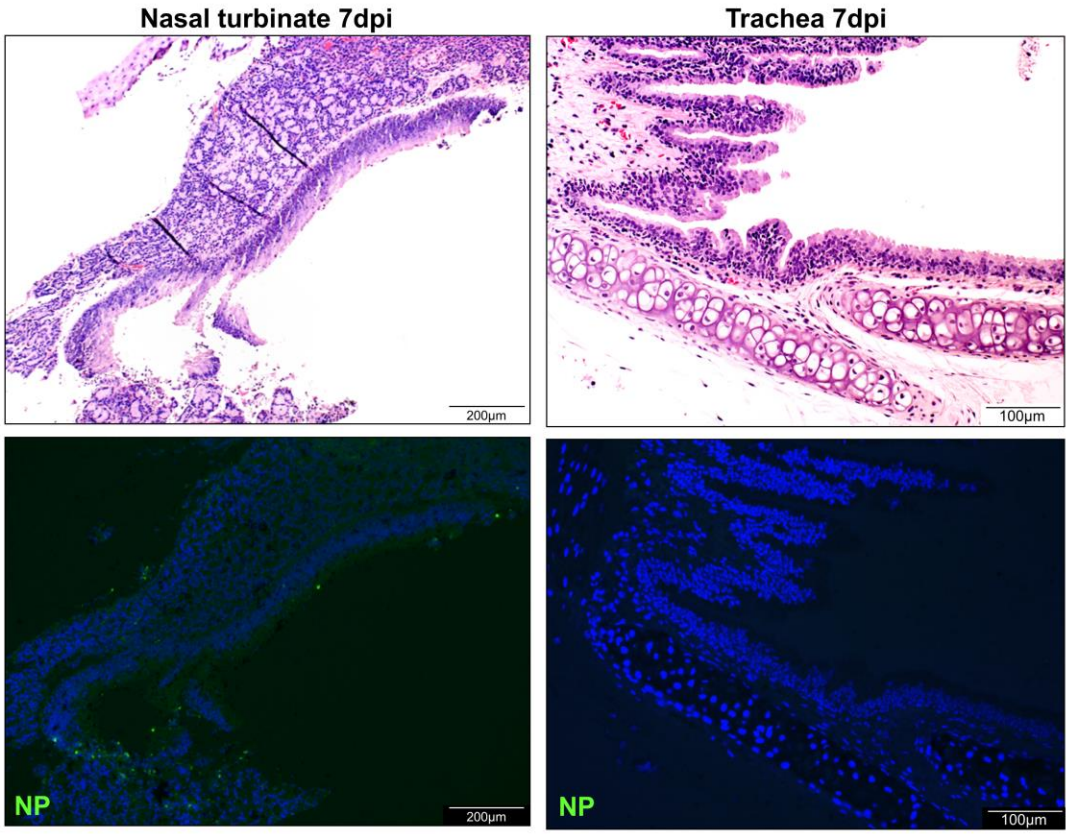

Figure 4B

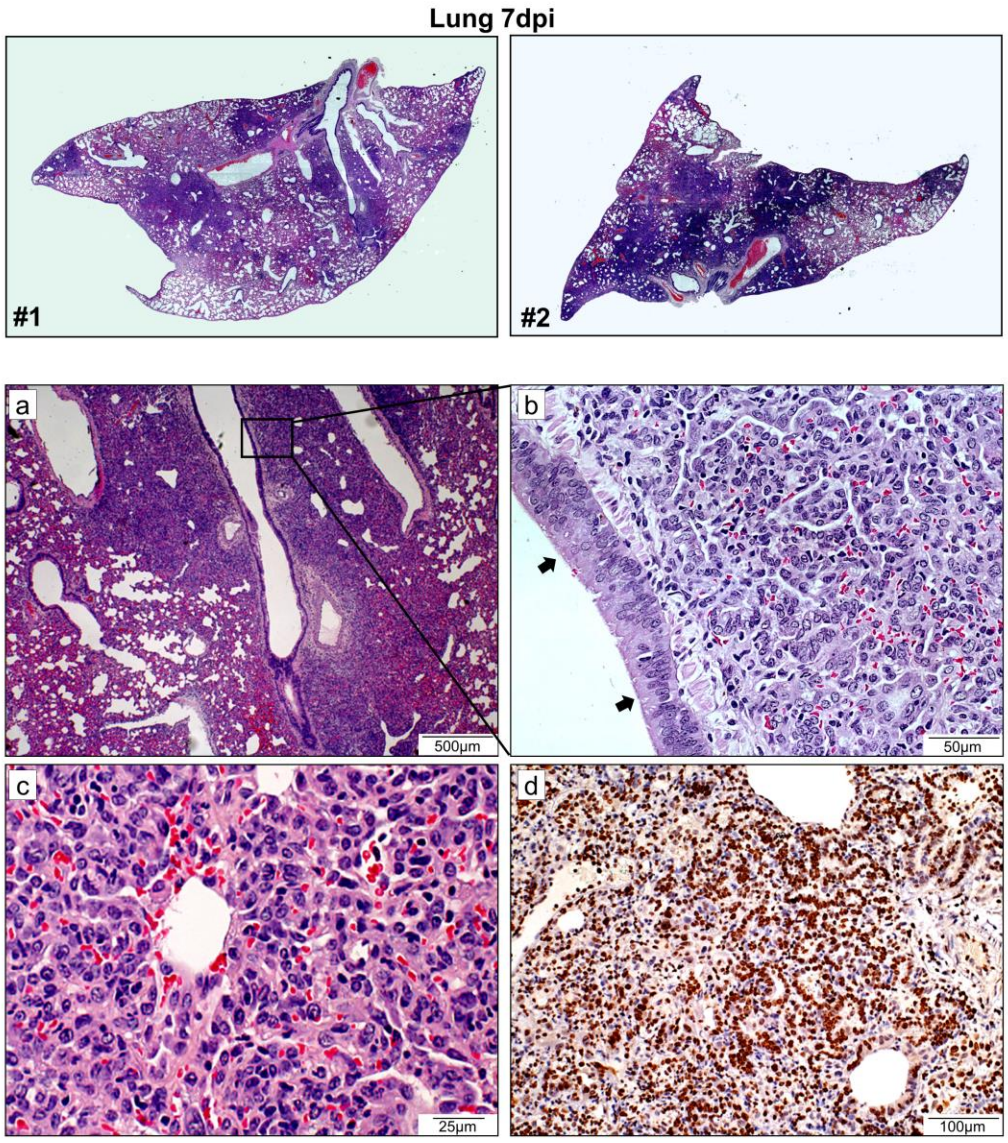

Figure 4B

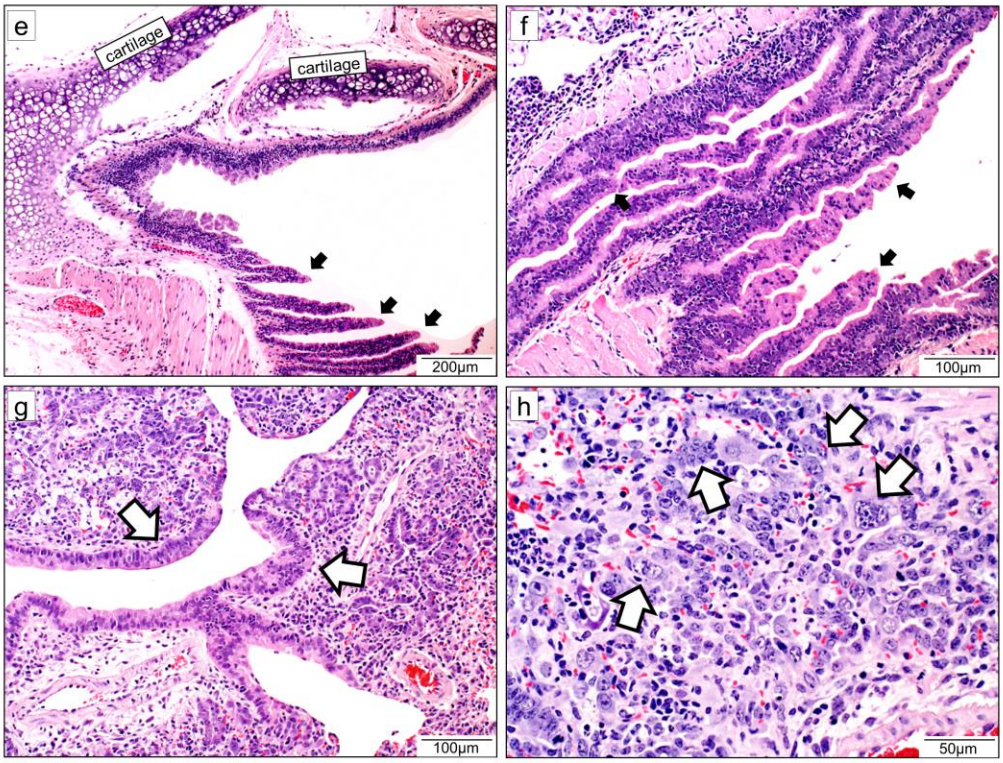

Figure 4C

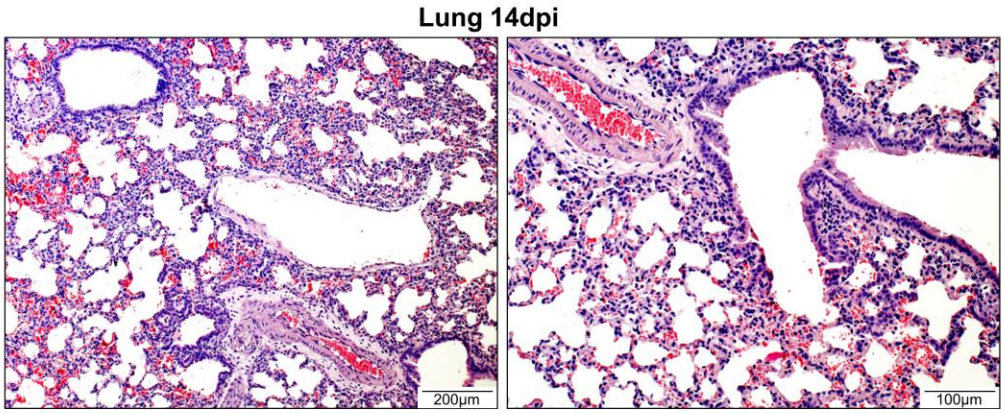

Figure 5A

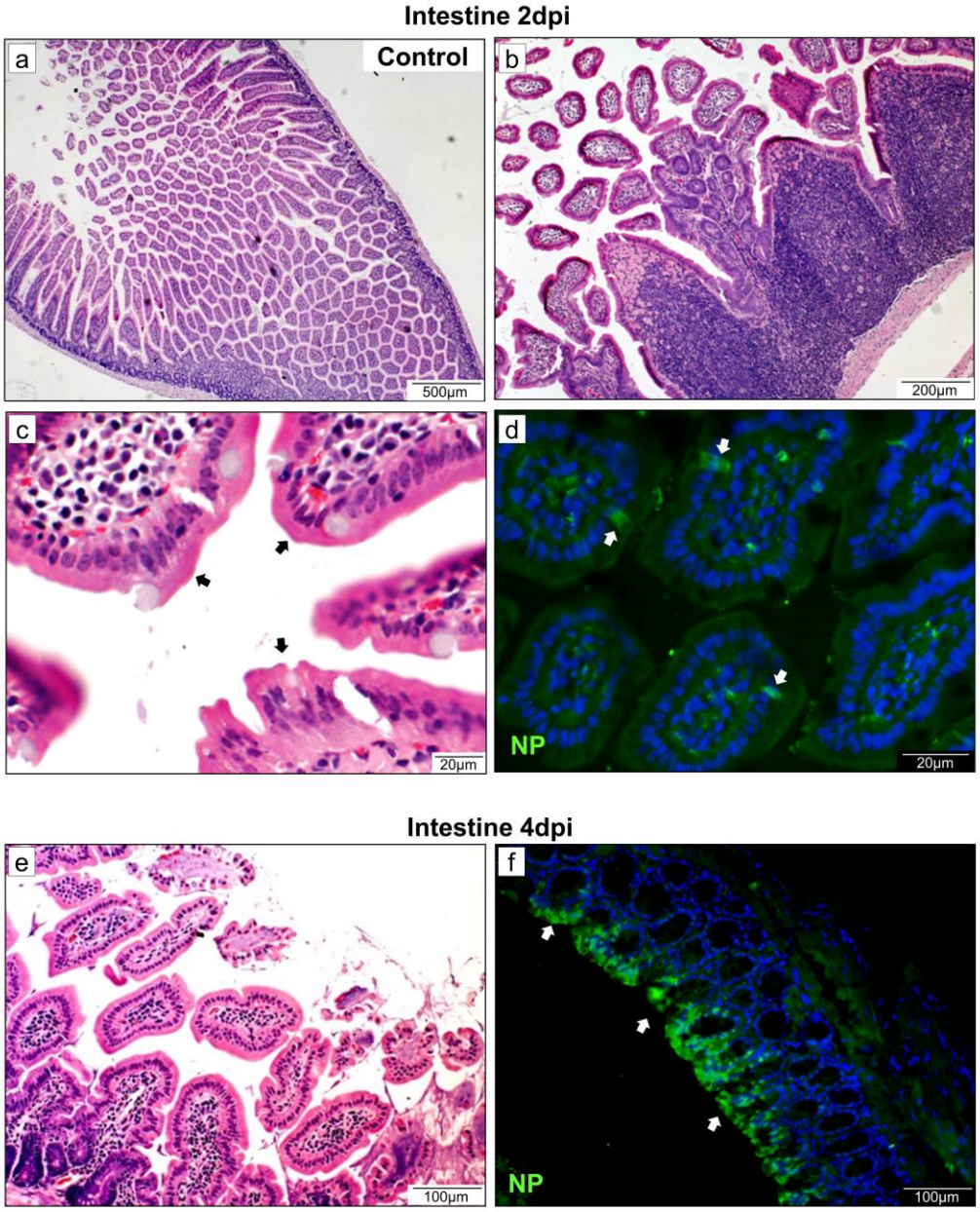

Figure 5B

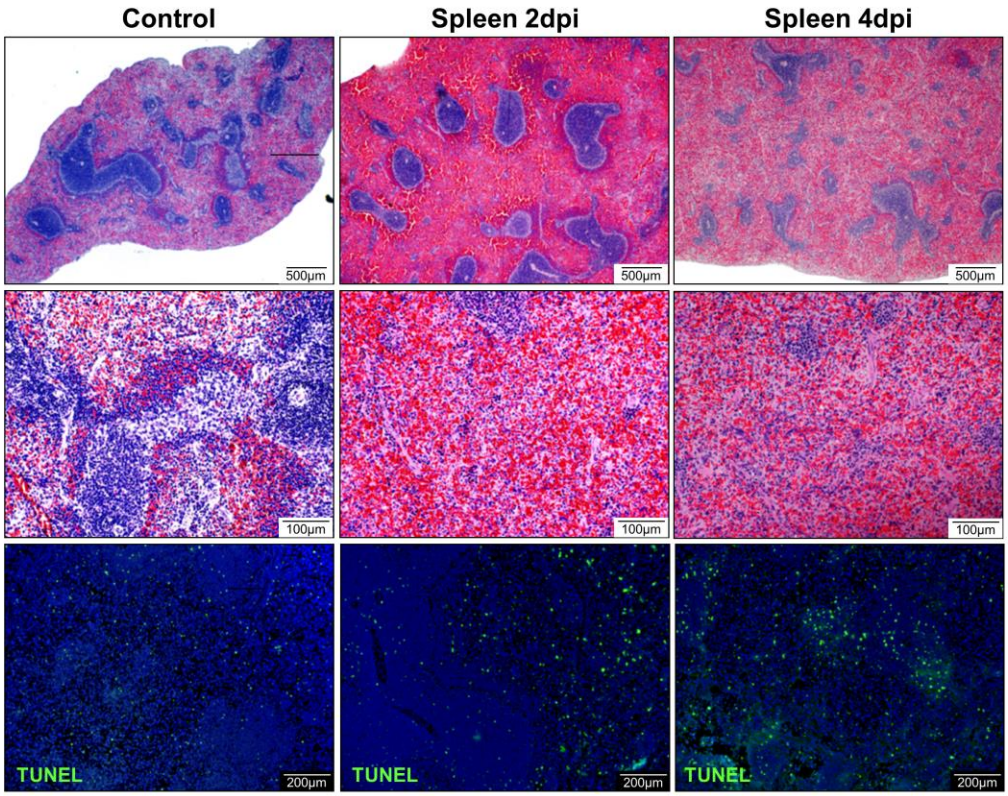

Figure 6A

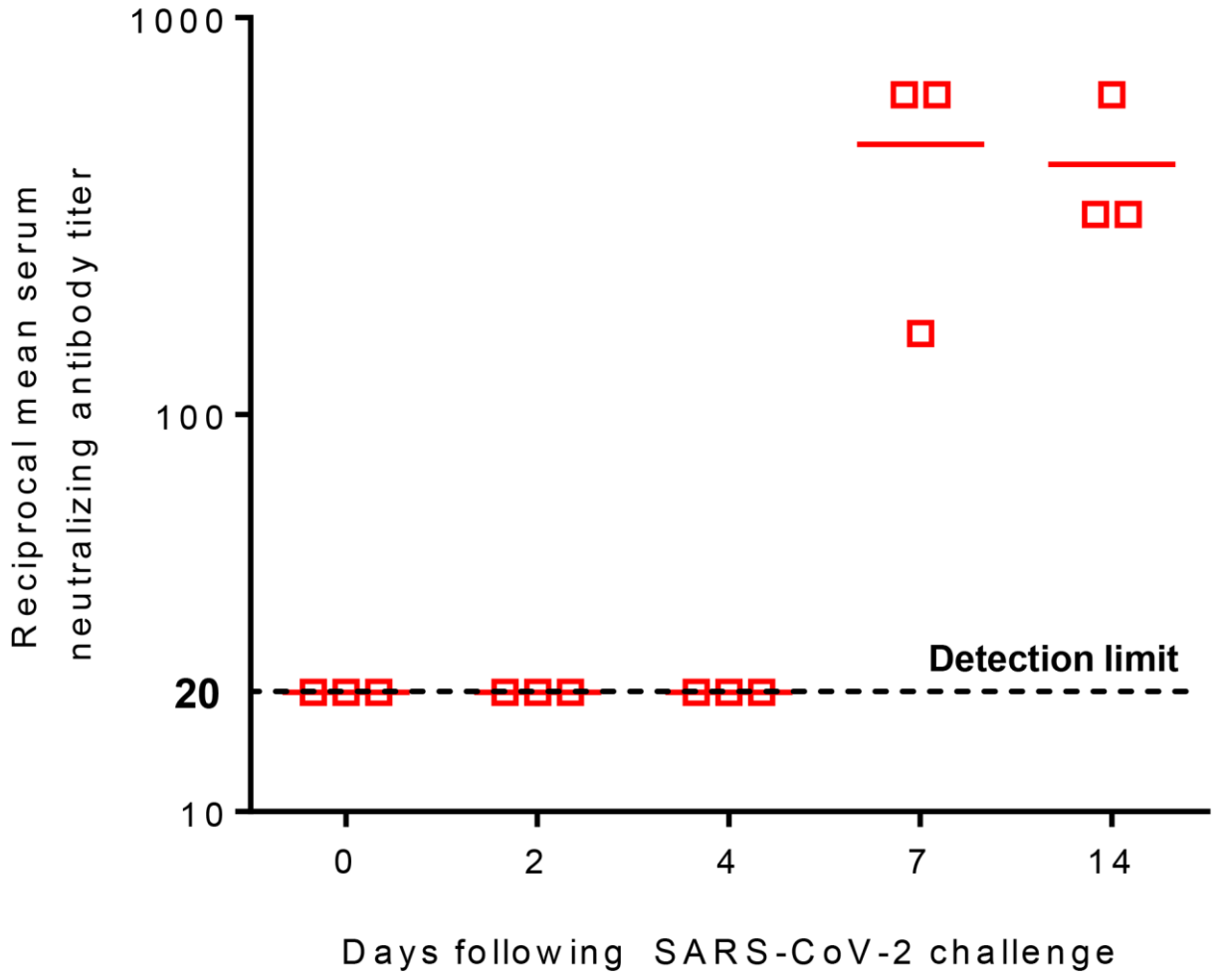

Figure 6B

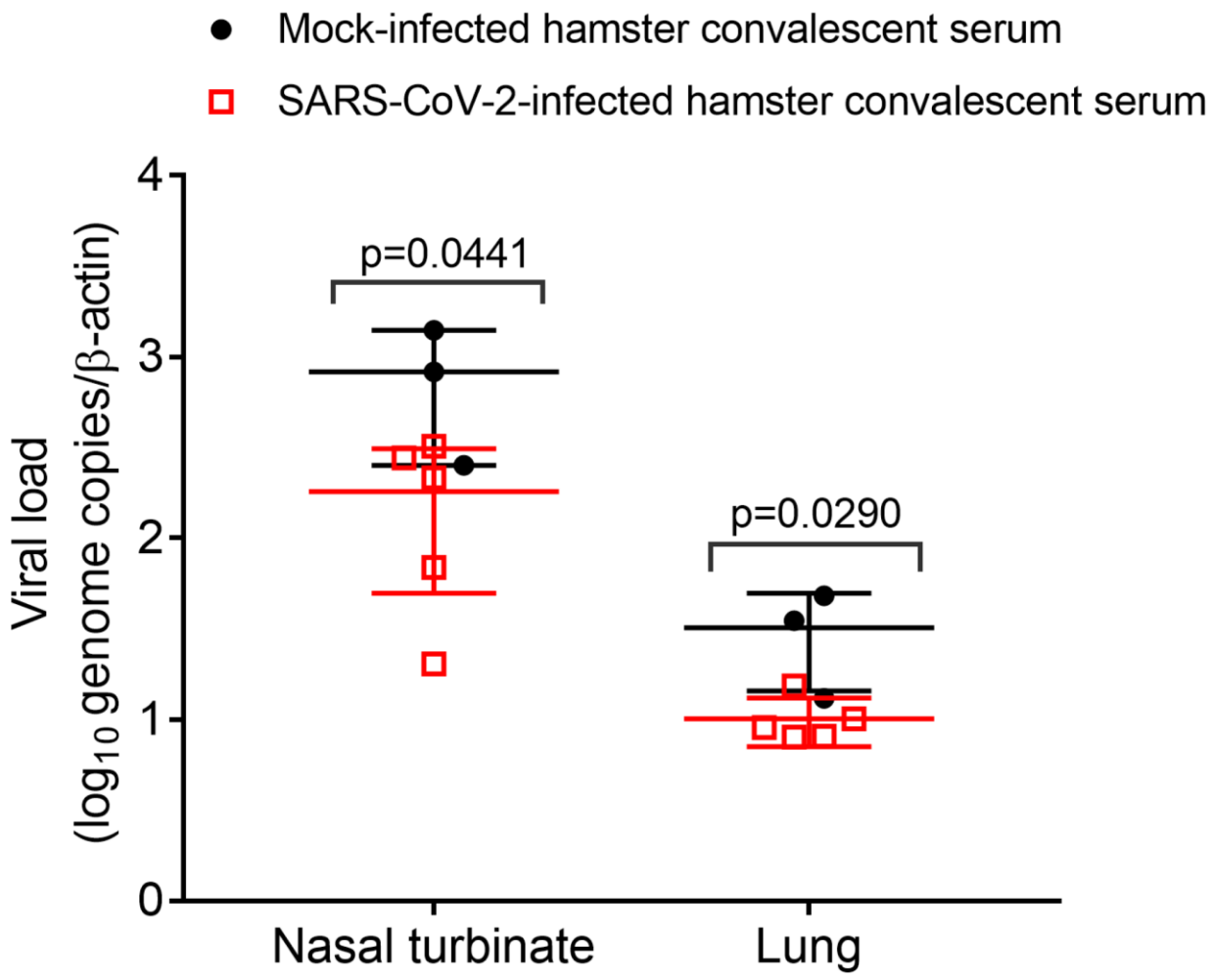

Figure 6C

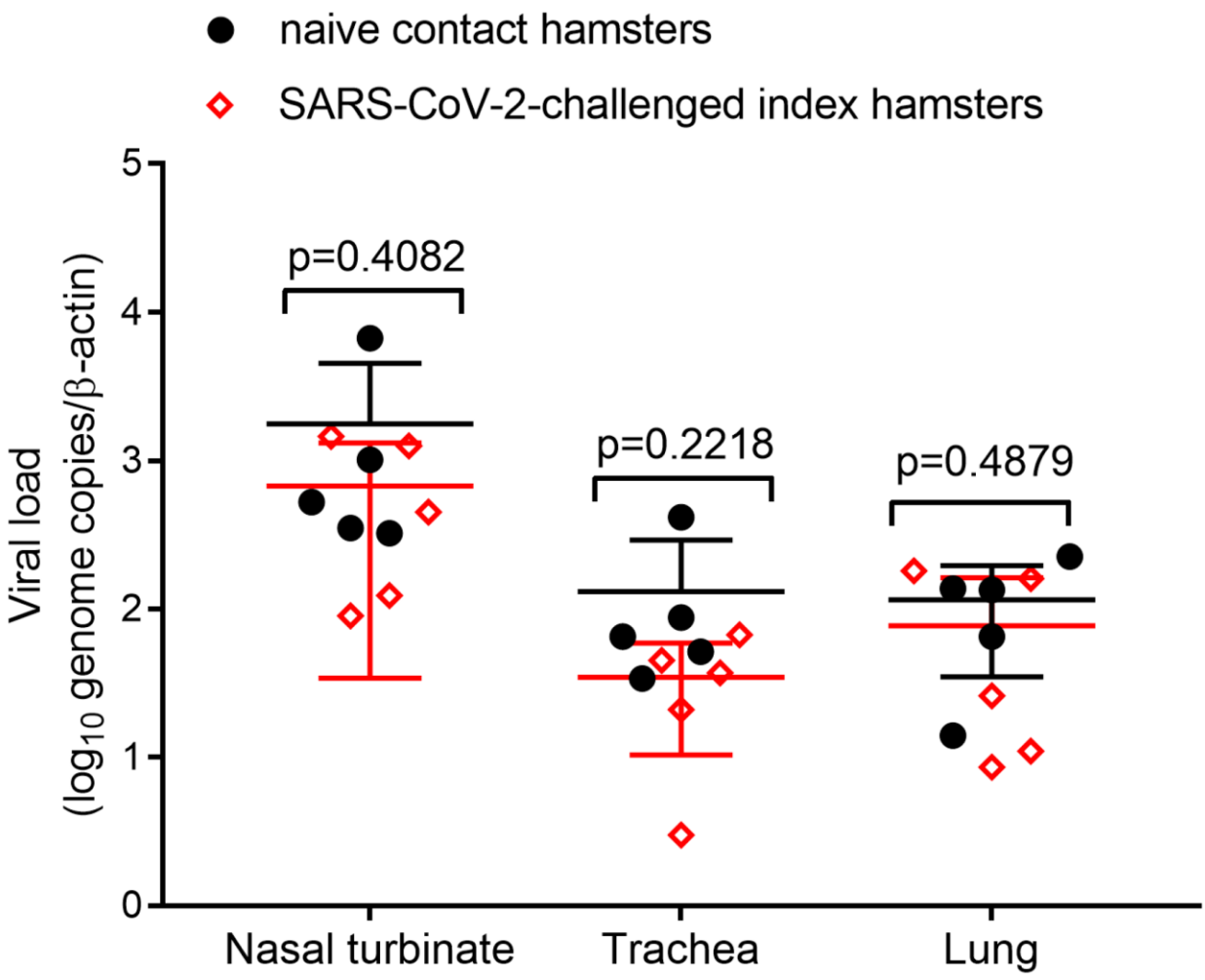

Figure 6D

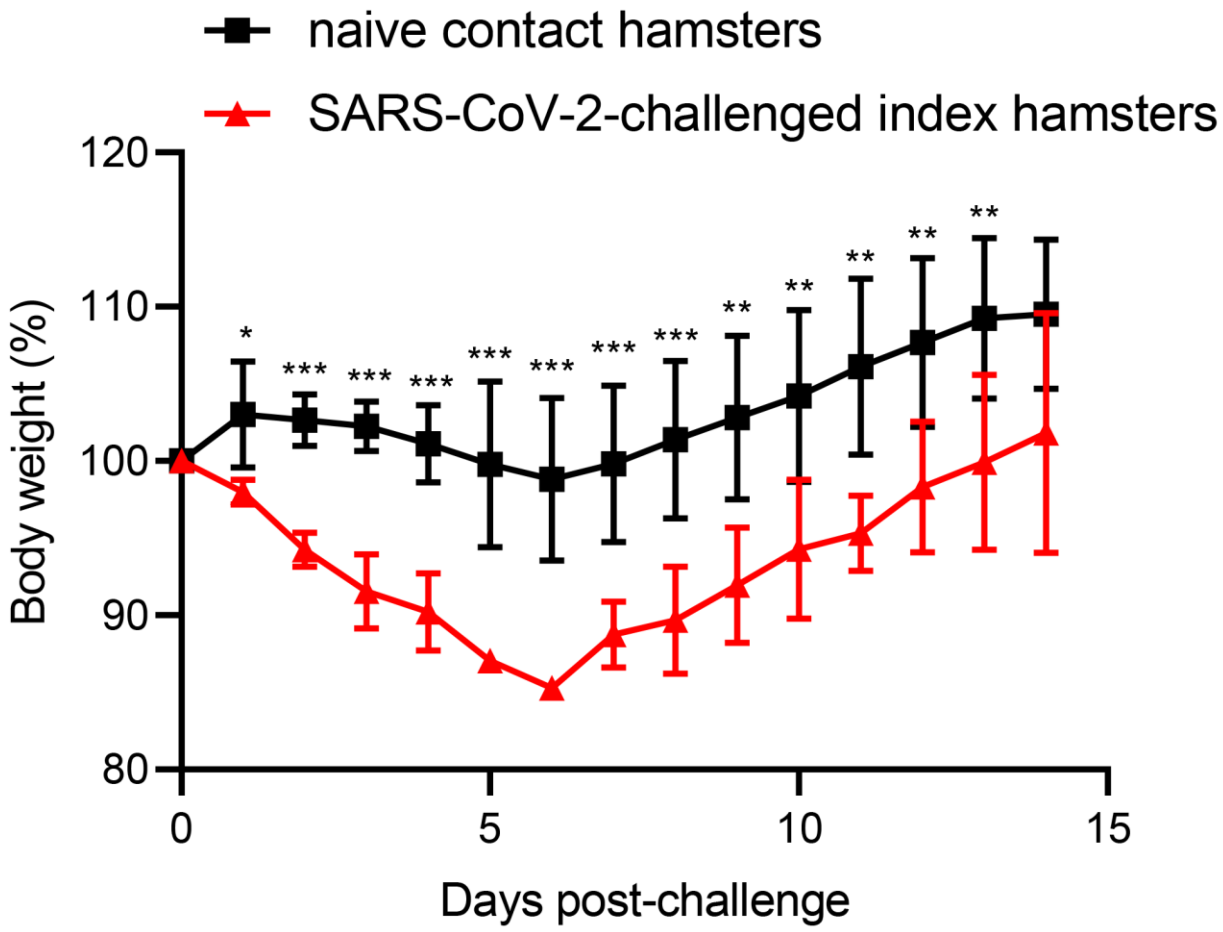

Figure 6E

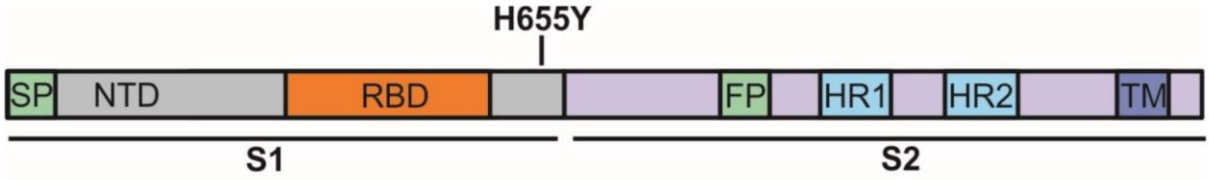

Animal	Spike position (nucleotide)		Amino acid
challenged index hamster 1	21	(TTA)	L7
challenged index hamster 2	21	(TTA)	L7
challenged index hamster 3	21	(TTA)	L7
naive contact hamster 1	21	(TTA)	L7
naive contact hamster 2	21	(TTA)	L7
naive contact hamster 3	21	(TTA/G)	L7
challenged index hamster 1	726	(CTT)	L242
challenged index hamster 2	726	(CTT)	L242
challenged index hamster 3	726	(CTT)	L242
naive contact hamster 1	726	(CTT/C)	L242
naive contact hamster 2	726	(CTT)	L242
naive contact hamster 3	726	(CTT)	L242
challenged index hamster 1	1176	(TTT)	F392
challenged index hamster 2	1176	(TTT)	F392
challenged index hamster 3	1176	(TTT)	F392
naive contact hamster 1	1176	(TTT)	F392
naive contact hamster 2	1176	(TTT)	F392
naive contact hamster 3	1176	(TTT/C)	F392
challenged index hamster 1	1963	(CAT)	H655
challenged index hamster 2	1963	(CAT)	H655
challenged index hamster 3	1963	(CAT)	H655
naive contact hamster 1	1963	(TAT)	Y655
naive contact hamster 2	1963	(CAT)	H655
naive contact hamster 3	1963	(CAT)	H655